Stress Balance in Synthetic Serpentinized Peridotites Deformed at Subduction Zone Pressures

Nadege Hilairet, J. Guignard, T. P. Ferrand, Sébastien Merkel, Paul Raterron, B. Ildefonse, Alexandre Fadel, W. Crichton

Stress balance in synthetic serpentinized peridotites deformed at subduction zone pressures

N. Hilairet[1], J. Guignard[2, *], T. P. Ferrand[3,4], S. Merkel[1], P. Raterron[1, ‡], B. Ildefonse[5], A. Fadel[6], W. Crichton[2]

[1] Univ. Lille, CNRS, INRAE, Centrale Lille, UMR 8207 - UMET - Unité Matériaux et Transformations, F-59000 Lille, France

[2] ESRF European Synchrotron, F-38000 Grenoble, France

[3] PSL Research University, Laboratoire de Geologie, Ecole Normale Supérieure, CNRS UMR 8538, F-75005 Paris, France

[4] Institute of Geological Sciences, Freie Universität Berlin, Malteserstr. 74-100, 12249 Berlin, Germany

[5] Geosciences Montpellier, University of Montpellier, CNRS, F-34095 Montpellier, France

[6] Univ. Lille, CNRS, INRAE, Centrale Lille, Université d'Artois, FR 2638 - IMEC - Institut Michel-Eugène Chevreul, F-59000 Lille, France

Corresponding author: Nadège Hilairet (nadege.hilairet@univ-lille.fr)

* now at IROX Technology, Toulouse, France.

‡ now at National Science Foundation, 2415 Eisenhower Avenue, Alexandria, Virginia 22314, USA

Key Points:

- In-situ stresses within antigorite+olivine aggregates deformed under high pressures and temperatures
- Stress partitionning changes with a threshold between 10 and 20 % antigorite volume fraction
- Olivine controls stress before this threshold and the aggregate hardens relative to pure olivine.

Abstract

Weak serpentine minerals affect the mechanical behavior of serpentinized peridotites at depth, and may play a significant role in deformation localization within subduction zones, at local or regional scale. Mixtures of olivine with 5, 10, 20 and 50 vol. % fraction of antigorite, proxies for serpentinized peridotites, were deformed in axial shortening geometry under high pressures (ca. 2 GPa to 5 GPa) and moderate temperatures (ca. 350°C), with in-situ stress and strain measurements using synchrotron X-rays. We evaluate the average partitionning of stresses at the grains scale within each phase (mineral) of the aggregate and compare with pure olivine aggregates in the same conditions. The in-situ stress balance is different between low antigorite contents up to 10 vol. %, and higher contents above 20 vol. %. Microstructure and stress levels suggest the deformation mechanisms under these experimental conditions are akin to (semi)brittle and frictional processes. Unlike when close to dehydration temperatures, hardening of the aggregate is observed at low serpentine fractions, due to an increase in local stress concentrations. Below and above the 10-20 vol. % threshold, the stress state in the aggregate corresponds to friction laws already measured for pure olivine aggregates and pure antigorite aggregates respectively. As expected, the behavior of the two-phase aggregate does not evolve as calculated from simple iso-stress or iso-strain bounds, and calls for more advanced physical models of two-phase mixtures.

Plain Language Summary

In subduction zones, a tectonic plate plunges beneath another one, and result in large mechanical stresses. These conditions can lead to earthquakes or ground displacements observable at human timescales. Measuring how viscous the rocks within subduction zones are, may help understand these events. Serpentinite are rocks from subduction zones which contain a variable amount of a weak minerals, including serpentine, and other stronger minerals. Using deformation experiments this study seeks to measure serpentinites viscosity, as a function of the amount of serpentine. At low serpentine content (at least up to 10%, but lower than 20 vol.%) and under temperature relevant for cold subduction zones, we found that the rock remains as hard as the strongest mineral which bears the whole load, and can even become harder because of grain-scale stress concentrations. At 50% volume fraction of serpentine, the rock has the same viscosity as serpentine itself. These measurements may for instance help larger scale numerical models of interseismic processes that happen between earthquakes, in subduction zones.

1 Introduction

Understanding strain localization processes within subduction zones, from long timescales (convection) to intermediate scales (slow slip events over hours or days), to short events (earthquakes) has become of major importance for our global picture of subduction zones dynamics. However, the strain rates and the stress balance at the interface between the slab and the mantle wedge, as well as those in the inner part of the subducting slab, remain poorly quantified. Rheological contrasts between different lithologies are decisive for the dynamics at the interface, including the exhumation of high pressure rocks (e.g., Agard et al., 2018 for a review, Schwartz et al., 2001, Federico et al., 2007), as well as seismicity (e.g. Ferrand, 2019,

observations in Abers et al., 2013) and mantle wedge flow (e.g. Abers et al., 2006, Wada et al., 2008). Knowledge of the rheology of subduction zones lithologies is thus required in order to decipher their histories and present-day processes.

Serpentinized rocks have long been proposed to strongly influence subduction zones dynamics, through a low mechanical strength (e.g., Guillot et al., 2015 and ref. therein, Schwartz et al., 2001). Serpentinization is a partial or total replacement of the most abundant silicate in peridotites, olivine, and pyroxene to a lesser extent, as a result of hydration. Antigorite, the high-pressure, high-temperature (above ca. 300°C) variety of serpentine (e.g., Evans, 2004; Schwartz et al., 2013) is potentially widespread in the mantle above the subduction interface, where fluids are released by progressive dehydration of hydrous phases in the subduting slab (e.g., Schmidt and Poli, 1998).

The rheological behavior of fresh dunite and peridotites, or olivine aggregates under high pressure - low temperatures below and up to 600°C, has been investigated for decades (e.g., Gaboriaud et al., 1981; Shimada, 1993; Raterron et al., 2004; Boettcher et al., 2007; Long et al., 2011, Druiventak et al. 2011, Proietti et al 2016, Mei et al, 2010). The rheology of serpentine aggregates and natural serpentinites has been studied under pressures up to 4 GPa and from ambient temperature up to dehydration temperatures (e.g., Escartin et al., 1997; Hilairet et al., 2007; Chernak and Hirth, 2010; Proctor and Hirth, 2016; Hirauchi et al, 2020; Shao et al, 2021, Burdette and Hirth, 2022). At single-crystal scale, olivine mechanical properties have also been investigated under low temperatures (e.g. Evans and Goetze, 1979; Gaboriaud et al., 1981; Kranjc et al., 2016; Kumamoto et al., 2017, Idrissi et al, 2016), and more recently those of antigorite (Hansen et al., 2020; Idrissi et al., 2020).

On the other hand, the mechanical behavior of serpentinized rocks has not been systematically investigated. Experiments have been carried out mostly under pressures below 2 GPa on the low temperature serpentine varieties lizardite and chrysotile (e.g. Escartin et al., 2001). High pressure experiments on antigorite-olivine aggregates or antigorite-rich serpentinites have mostly been targeted at antigorite dehydration conditions, owing to its potential link with subduction zone seismicity (e.g. Dobson et al, 2002; Jung et al, 2004; Xia et al, 2013; Chernak and Hirth, 2011; Gasc et al, 2011; Gasc et al, 2017; Ferrand, 2017; Ferrand et al, 2017).

Olivine and serpentine have different intrinsic elastic and crystal-plastic properties. Therefore the resulting elastic and plastic properties of the serpentinites may not be easily predicted from the end-members (in the following, 'plastic properties' refers to crystal plastic properties unless otherwise stated). Burnley (2013) for instance, modeled how contrasts in elastic and plastic properties can lead to variable local stress states, due to stress percolation.

Microstructure is also expected to influence stress distribution throughout a deforming two-phase aggregate. Indeed, serpentinites can be found within heterogeneously deformed shear zones and tend to have strong preferred orientations (e.g., Nishii et al., 2011; Padron-Navarta et al., 2012; Morales et al., 2018). Handy (1990, 1994), laid out a conceptual framework with two end-members 1) the strongest phase controls the stress through a load-bearing framework 2) the weakest phase controls deformation because it is spatially connected, being either abundant enough to be connected prior to deformation, or becoming connected through increasing strain amount. More recently Gerbi et al., (2016), underlined that beyond the simple connectivity of weak phases in natural rocks, developement of weak zones bridging the weak phase can control the aggregate strength.

Analytical mixing models, ranging from simple end-member models to more complex models, do exist for flow laws (e.g., Tullis et al, 1991, Takeda, 1998, Huet et al, 2014), but are not easily applicable when frictional processes and semi-brittle deformation occur. A whealth of numerical studies on two-phase geological aggregates is available in the literature, based one way or the other on Finite Elements Models (e.g. Tullis et al, 1991, Madi et al, 2005, Jessell, et al, 2009, Cook et al, 2014, Cyprych et al., 2016), sometimes combined with mean-field or analytical approches (e.g. Canova et al., 1992, Thielmann et al., 2020). These numerical models remain costly computationally and need anchoring on observables and experimental work in order to be relevant and well-targeted. Experimental mapping of physical (pressure, temperature, strain rate, strain) and microstructural conditions for specific deformation regimes of serpentinites is therefore necessary.

A number of studies have taken advantage of high-pressure deformation experiments with in-situ synchrotron X-ray measurements in two-phase mineralogical assemblages, which allow to investigate the stress partitioning between the different phases (Li et al., 2007; Wang et al., 2013; Girard et al., 2016; Kaercher et al., 2016; Farla et al., 2017; Lin et al., 2019, Tokle, et

al., 2021). We present here an experimental study of the effect of serpentine fraction within a mixture of olivine+antigorite, on the mechanical behavior of the aggregate. The deformation experiments were carried out under high pressure and high temperature, in axisymmetric shortening (pure shear). Using *in situ* stresses and strain measurements, here we evaluate the partitionning of stresses within each phase (mineral) of the aggregate. These results show two distinct regimes for stress partitioning as a function of the antigorite volume fraction, with different mechanisms for stress control.

2 Methods

The deformation experiments were carried out in the D-DIA large-volume press at ID6-LVP at the European Synchrotron Radiation Facility in Grenoble, France (Guignard and Crichton, 2015). A monochromatic beam with a wavelength corresponding to 33 keV was used, with a beam size of ca. 1 mm wide by 0.5 mm height.

The samples were powders ground and mixed from natural San Carlos olivine and antigorite from Corsica, used in Ferrand et al. (2017) and Ferrand (2017) with 5, 10, 20 and 50 vol. % antigorite. The powders were sieved for grain sizes below ca. 30 microns. Upon compression under high pressure (P) and high temperature (T) (1.5 GPa, 773K), the resulting aggregates display a rather homogeneous distribution of the phases (Ferrand, 2017). Antigorite is distributed in patches, referred to as “clusters” in Ferrand et al. (2017), that become connected at the highest antigorite fraction. In the present experiments the mixtures were hand-pressed and directly loaded within the high-pressure cells.

Anvils with 6 mm truncation were used, made of tungsten carbide on the upstream side and sintered diamond (SD) on the downstream side, for recovering full angular dispersive diffraction patterns. 9 mm edge cubic cells were used (figure S1), with amorphous B+epoxy as pressure medium, a graphite furnace, porous alumina pistons, and zirconia plugs for thermal insulation. In each run, two samples were stacked in the cell: ca. 1.5 mm height, pure olivine powder, and ca. 1.5 mm height, two-phase powder (antigorite + olivine). The pure olivine powder is used as a reference in the same P and T conditions as each two-phase aggregate, in order to compare runs between themselves. All samples were separated from one another and from the pistons by 20 microns-thick gold foils.

The samples were compressed at a target load of 30 bars, intended to reach hydrostatic P ca. 3 GPa (not always reached, see table 1). The temperature was imposed by a current circulating through a graphite furnace and estimated from an off-line calibration, between 395 and 420°C at the beginning. The shortening of the assembly during deformation in the D-DIA can induce changes in the T gradient (Raterron et al., 2013). Based on their results (at 1673 K, much higher than the present study) and the total length of our samples, here a temperature of 300 to 350°C is assumed. The stresses built-up during compression were relaxed at the run T for about 1 hour prior to deformation. The samples were then shortened up to the final strain, quenched and decompressed, and finally recovered for SEM analysis.

Sample axial strains were measured using X-ray radiography. Due to the x-ray beam height of 0.5 mm, the samples stacks were scanned in the vertical direction to take a series of 12 or more images, and the full image was reconstructed. One full image was typically acquired over a few seconds, which remains very short with respect to the speed of deformation. The strain is defined as $\varepsilon = ln(l/ l_0)$, l being the sample length and l_0 the reference length taken at the beginning of the deformation (start of differential rams). The experiments were carried out at strain rates around 10^{-5} s^{-1} and total strains up to ca. 30% (Table 1).

2D X-ray diffraction (XRD) patterns were collected on a rotating linear 1-D detector (see Guignard and Crichton, 2015, for details), with a typical acquisition time of the order of 1 minute for a 360° full azimuthal acquisition. The detector tilt and rotation relative to the incident beam were calibrated with a LaB_6 standard using Fit2D (Hammersley, 2016). The 2D diffractions allowed recovering stresses within phases in the single-phase and two-phase samples for each run. The full framework for these analyses has been widely presented in the literature (e.g., Uchida et al., 1996; Singh et al., 1998). For a polycrystal under differential stress, departure of the powder diffraction pattern from ideal rings can be used as a proxy for the supported differential stress. This departure is referred to as “lattice strain”, noted *Q(hkl)* for the *hkl* diffraction line. The isotropic component of the stress tensor (the mean stress), hereafter called either pressure (P) or mean stress, can also be recovered. The analysis was carried out using the Multifit – Polydefix software available online at http://merkel.zoneo.net/Multifit-Polydefix/ (Merkel and Hilairet, 2015).

184 P was calculated using a thermal equation of state for San Carlos olivine (Guyot et al.,
185 1996) in the reference sample and in the two-phase sample. Both were fairly consistent (table 1).
186 Antigorite d-spacings were not converted to pressures because only one diffraction plane with
187 robust information was available.

188 Converting lattice strains into macroscropic stresses is not straightforward (see Chen et
189 al, 2006, Burnley and Zhang, 2008, Merkel et al, 2009 for a full discussion, and Hilairet et al,
190 2011 on olivine specifically). Lattice strains from the 021, 101, 130, 131 and 112 diffraction
191 lines (pbnm setting is used throughout the manuscript) were recovered for olivine in both the
192 single-phase aggregates and in the two-phase aggregates. The stresses were calculated from
193 different *Q(hkl)* using elastic stiffness tensors (C_{ij}) at the relevant P and T (Isaak, 1992; Zha et
194 al., 1996) assuming a constant stress hypothesis (Uchida et al., 1996; Singh et al., 1998). This
195 leads to a spread of stresses calculated from different crystallographic planes, which are then
196 averaged to represent the aggregate stress. This averaging represents the main limitation of *in*
197 *situ* stress measurements based on XRD, as it has no theoretical grounds and does not take into
198 account plastic relaxation occuring within the sample. As of today, there is no satisfactory way to
199 obtain the stress uncertainty. Elasto-Visco-Plastic Self-Consistent (EVPSC) modeling of the data
200 has been proposed as an answer to this pitfall (Burnley and Zhang, 2008; Burnley, 2015). The
201 implementation of relevant mechanisms for olivine deformation into these codes, however, is
202 still uncomplete (Hilairet et al., 2011; Burnley, 2015). We believe some precautions ensure that
203 relative comparisons can still be made out of these measurements. First, the deformation curves
204 for the four runs display the same relative evolutions for the different planes (not shown), and we
205 compare here averages from the same lattice strains. Second, the texture of the olivine in the
206 aggregates is weak and the diffraction lines include many more crystal orientations than in a
207 strongly textured case. The planes (021), (101), (130), (131) and (112) cover the three main
208 lattice directions in olivine, hence the average is not biased by underrepresented directions of the
209 unit cell.

210 For antigorite, we recovered lattice strains for the 001 diffraction lines for all two-phase
211 samples. Only pressure dependencies of C_{ij} for antigorite are available (Bezacier et al., 2010).
212 The expected effect of increasing T would be opposite effect to that of P. Therefore C_{ij} at
213 ambient P and T were used. This also allows to keep consistency with previous results on
214 antigorite aggregates (Hilairet et al., 2007). Using C_{ij} at 3 GPa and ambient T increases the

calculated t(hkl) stresses by about 15%, which provides an upper bound for the interpretation of the results.

3 Results

The main results from in-situ measurements are summarized in table 1. Olivine and antigorite are referred to as 'ol' and 'atg' in the table and figures.

Table 1. Summary of experimental runs conditions.

run #	atg vol. % in two phase aggr.	Strain rate ref.	final strain ref.	Strain rate two-phase aggr.	final strain two-phase s aggr.	σ_{ol} ref. (GPa)[a]	P ref. (GPa)[b]	σ_{ol} two-phase aggr. (GPa)[a]	P two-phase aggr. (GPa)[b]	$\sigma_{atg\ (001)}$ (GPa)	peak $\sigma_{atg(001)}$ (GPa)
serp6	0.05	-1.99E-05	-0.23	-1.58E-05	-0.20	3.78	4.86	3.69	4.91	1.06	2.18
serp7	0.1	-1.43E-05	-0.25	-1.66E-05	-0.29	3.73	4.00	3.49	4.00	1.68	2.58
serp9	0.2	-1.17E-05	-0.14	-4.52E-05	-0.27	3.23	1.89	3.02	1.78	2.84	2.84
serp10	0.5	-1.77E-05	-0.19	-3.61E-05	-0.34	3.25	3.18	2.67	3.17	2.64	2.64

[a] stress calculated from olivine diffraction planes

[b] P measured from olivine diffraction, given here at the final strain

3.1 *In-situ* strain rate

The strain rates of the two-phase aggregate with 5 and 10 vol. % and their respective reference aggregates are similar (fig. 1).

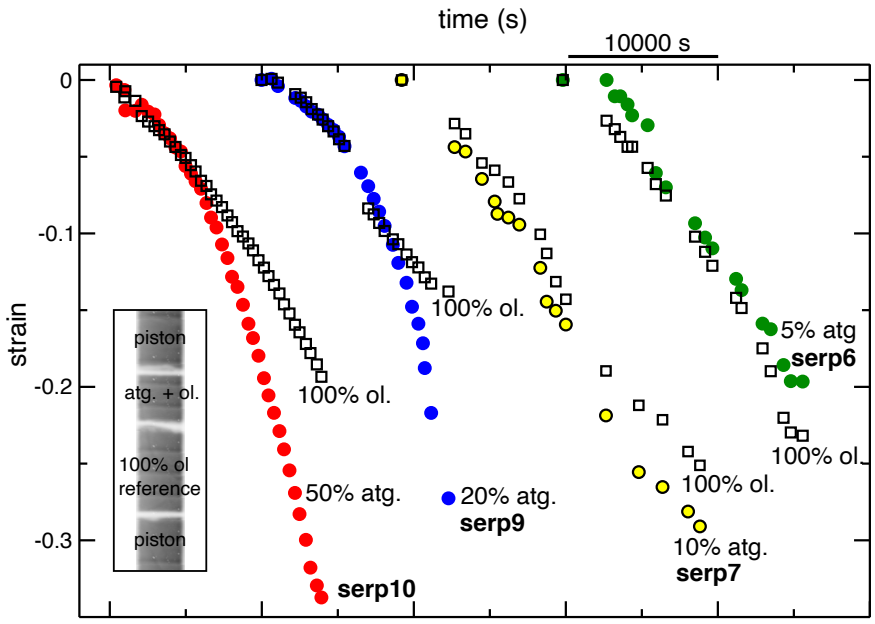

Figure 1. Strain evolution with time for the two-phase aggregates (filled symbols) and for the reference (100 vol. % olivine aggregate, empty squares). Each run (serp6, 7, 9, 10) had a reference aggregate in the column stack, as shown in the inset. The curves have been shifted one run from another on the time axis, for visibility. The scatter on runs serp6 and serp7 is due to the image analysis process, which was improved for runs serp 9 and serp10. The jump and change of slope seen on serp9 is real.

With 20 and 50 vol. % antigorite, the two-phase aggregates deformed faster than the reference aggregate. The speed of the differential rams was identical in all experiments (175 µm/hour). The scatter in runs serp6 and serp7 (two-phase and reference aggregate) is due to difficulties in reconstructing an image of the full sample column, from the series of images taken while scanning the column. However, the jump in strain in run serp9 on the olivine reference aggregate is real, and very likely related a failure in the reference aggregate. This is further examined in the discussion.

3.2 In-situ partitionning of stresses

The diffraction allows us to obtain stress information in each of the two minerals of the two-phase aggregates, which are reported in fig. 2 as stress-strain curves.

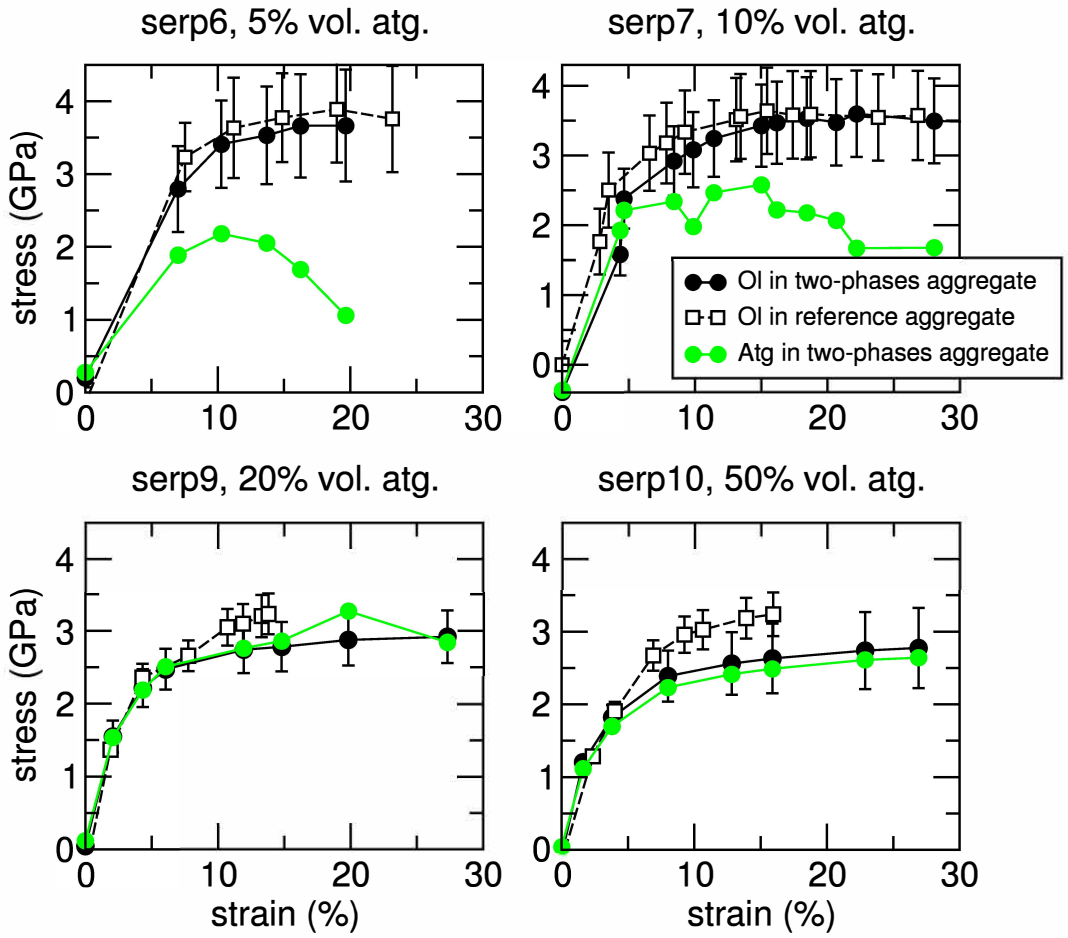

Figure 2. Stress partitioning as a function of strain measured in the olivine (ol, solid black circles) and antigorite (atg, green) of the two-phase aggregates, compared to stress - strain curve measured on the olivine single-phase reference aggregate (empty black squares) for each experiment. Stress was not measured for each strain step shown in fig. 1, therefore the final strain shown here can be different. For olivine the stress is calculated from averaging the stress measured on different crystallographic planes. The error from the diffraction fitting is typically the size of the symbols, the bars represent the standard deviation for the average stress (not an actual error on stress, see further information in the methods section). For antigorite, only one plane could be confidently analyzed.

Olivine *(hkl)* planes stresses calculated from available lattice strains *Q(hkl)* are averaged for clarity. Since the same diffraction planes are considered, and since *Q(hkl)* relative amplitudes remain similar, the averaged stresses from the two-phase and the reference agregates can be compared (also see methods section for stress uncertainty). For the antigorite bearing aggregates, only the basal 001 diffraction peak of antigorite could be confidently fitted. In the 5 vol. %

sample, as deformation proceeded the signal on this 001 diffraction line broadened and became too faint to be analyzed.

The 5 and 10 vol. % antigorite aggregates on one side, and the 20 and 50 vol. %. antigorite aggregates on the other side, show a different behavior of the (001) plane. The stress on (001) becomes similar to the olivine mean stress when the amount of serpentine is 20% or more. For antigorite-poor aggregates, the stress reaches a maximum and then decreases (fig. 2). The 001 peak then disappears for 5 vol. % antigorite sample, while with the 10 vol. % antigorite, it remains present and reaches a plateau.

3.3 Microstructures

In recovered samples, a wide range of brittle features are observed, from micro-cracking, to diffuse or single fracturation at sample scale, sometimes overprinted with unloading cracks. These features are present in single-phase and two-phase aggregates. See figure S2 for micrographs of recovered samples. Note the initial angle of any brittle feature generated under high pressure and high temperature may have been altered by the decompression stage, carried out under ambient temperature.

Back-scattered electron images (BSE) were obtained on the recovered samples. This work was carried out at the electron microscopy facility of the Advanced Characterization Platform of the Chevreul Institute, using a FLEXSEM 1000 scanning electron microscope (SEM): (fig. 3), a Hitachi SU 5000 under low-vacuum conditions (Fig. 4), and a JEOL JSM-7800F (Fig. S2). Olivine grain sizes in recovered samples range from less than a micron to an apparent equivalent diameter ca. 25-50 μm. BSE images in fig. 3 show the antigorite distribution relative to olivine grains.

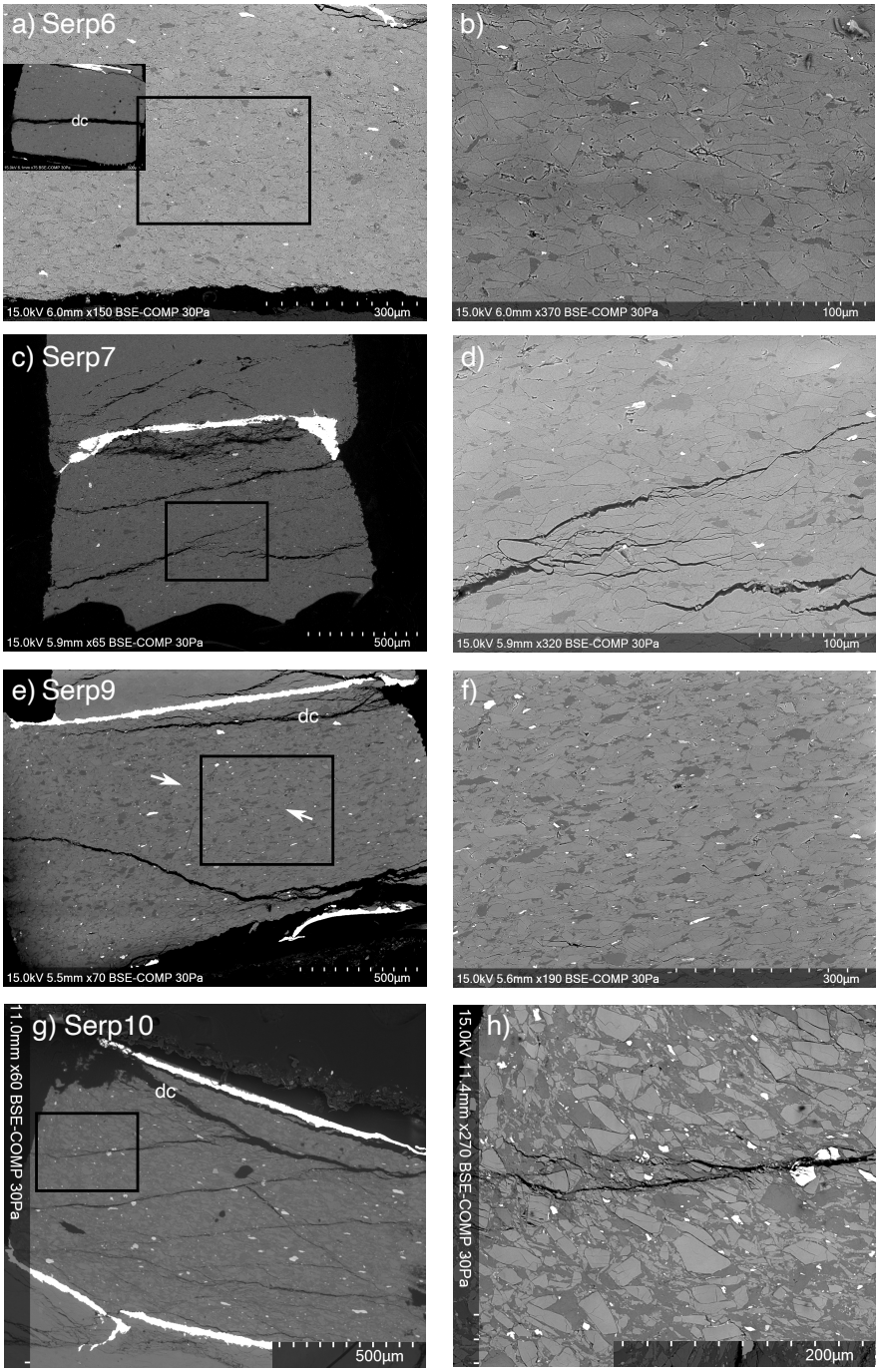

Figure 3. Electron microscopy (Back Scattered Electons) images of the recovered two-phase aggregates. The rectangles on the left column show the location of the smaller scale images on the right. Antigorite is dark grey on all images and olivine is light grey. The bright materials are the gold sheets used as strain markers, and iron oxydes naturally present in the starting powders. The bottom of Serp7 in c) is covered with conductive paste. dc = decompression crack. The white arrows in e) show an en-echelon distribution of clusters, which may play a major role in obtaining a stress controlled by antigorite without having an interconnected network.

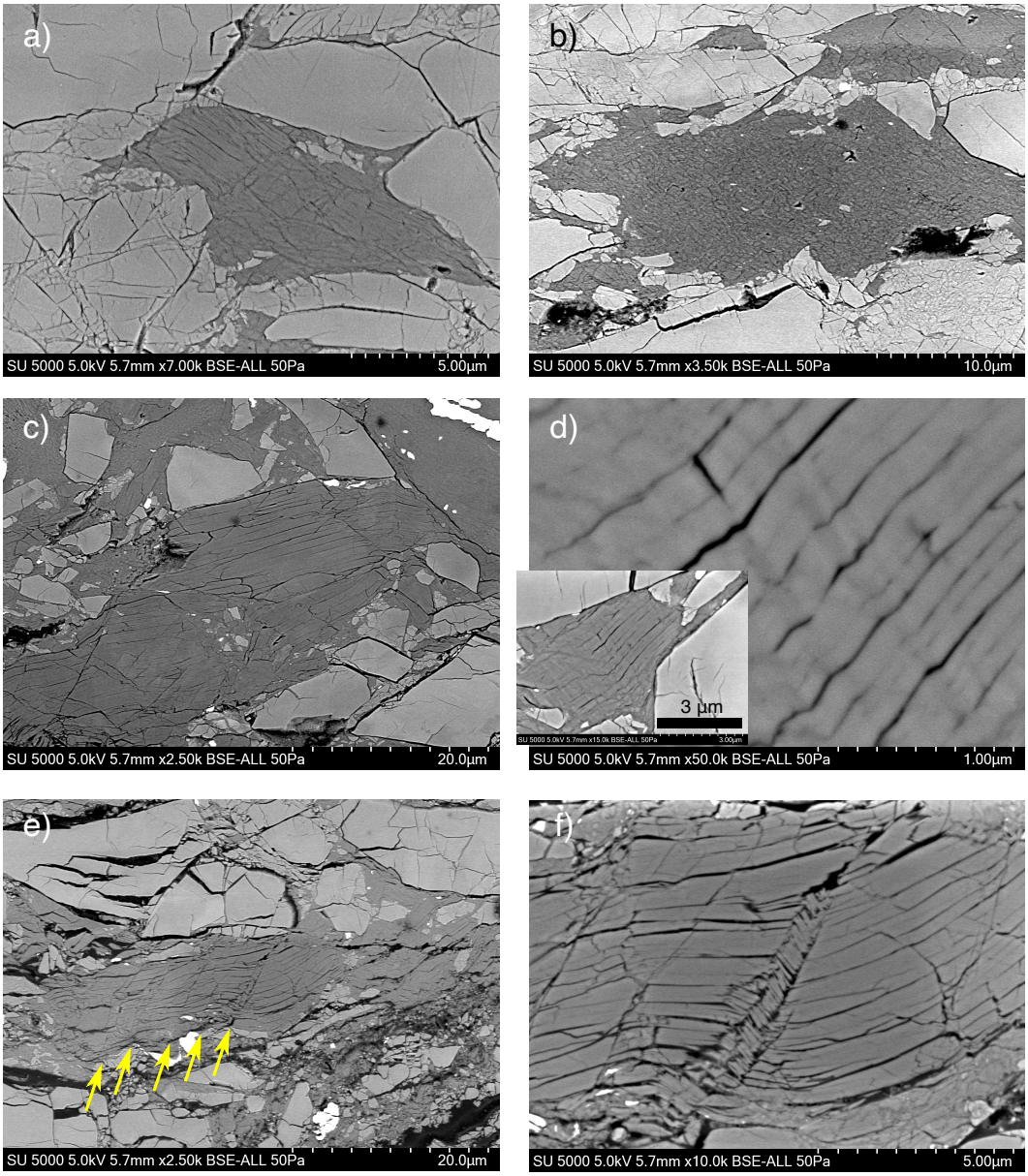

Figure 4. BSE images of deformation features in antigorite clusters, for 20% (a and b, serp9) and 50% (c, d, e, f, serp10) antigorite fraction samples. Antigorite is dark grey, olivine light grey and the bright phases are oxides. The maximum stress direction is vertical. In serp9 : a) antigorite crystal preserved with grain size reduction next to an olivine grain size reduction area and b) intense grain size reduction area. In serp10: c) large antigorite crystal preserved with an area of grain size reduction in the upper left part, d) kink bands at the 100-nm scale in response to local strain field imposed by the olivine crystals (inset), e) crystal deformed by a series of fractures and kinks with the same orientation (arrows) and bending, f) close up of the kink-band with loss of cohesion between sheets. Further images for 5 and 10% vol. antigorite, see figure S2.

Serp6 sample with 5 vol. % antigorite shows no obvious microcracking at the *aggregate* scale. Serp7 sample with 10 vol. % antigorite shows three oblique cracks which seem conjugated and could be related to deformation, without obvious displacements. Openings at grain boundaries, due to the decompression at the end of the run, highlight the cracks. At *crystal* scale olivine presents microcracking in both Serp6 and Serp7 (supplementary figure S3). Antigorite is distributed as isolated clusters throughout the sample. In these aggregates with 5 and 10% vol. antigorite (serp6, serp7), these clusters tend to have lower aspect ratio than those in the 20 vol. % antigorite sample (figures 3b, 3d).

Serp 9 with 20 vol. % antigorite, shows only one large crack, not conjugated and with no visible motion, and which geometry is ambiguous to interpret. The distribution of antigorite within the olivine matrix shows clusters of antigorite generally up to 90-100 μm of apparent length on the 2D section, at high angles or perpendicular to the maximum compression axis. One cluster up to 200 μm is observed. The deformation is heterogeneous with some clusters much less deformed in the upper left part of the sample on fig. 3e. As first glance they do not seem to be fully connected across the sample. However, a suite of an-echelon clusters, ca. 500 microns long, is observed in the central part (fig. 3e). The deformation style of antigorite clusters thus evolves with increasing antigorite fraction. The antigorite in the clusters themselves is preserved as crystals of a few microns, with grain size reduction often close to olivine grains (fig. 4a). Some regions with grain size reduction are observed in both in olivine and antigorite (fig. 4b).

Finally, in Serp10 with 50% antigorite, major brittle features allowed a homogeneously distributed (semi-)brittle deformation of the sample. They consist of a regular network of conjugated micro-fractures with a similar apparent angle from the maximum compression axis. At grain scale, the olivine crystals are angular, distributed within an antigorite matrix. Large crystals of antigorite can be preserved, and although grain size reduction is observed, it seems less developped than in serp9. The antigorite clusters deform by grain boundary slip, delamination, kink bands, fracturation, bending (fig. 4 d, e, f), in response to the local surroundings (relation with olivine crystals fig. 4e).

Reference aggregates in runs serp7 and serp9 display some regions with very small grain sizes (olivine), similar to those observed by Ferrand et al. (2017). Their cause, grain size

319 reduction during deformation or presence from the beginning of the run, is unclear. They are
320 found in olivine reference aggregates only.

321 The samples have also been investigated by Electron Back-Scattered Diffraction (EBSD)
322 – Scanning Electron Microscopy at the University of Montpellier, on the French CNRS-INSU
323 National EBSD Facility (CamScan Crystal probe). Regions, typically 400 by 500 μm, where
324 mapped for the reference and the two-phase aggregate for each run. Unfortunately, despite
325 several attempts, the EBSD signal on antigorite crystals could not be investigated. This is partly
326 due to the difficulty in polishing the surfaces with such a hardness contrast and with grain sizes
327 approaching the micron - a suitable way of preparing the samples remains to be found. Other
328 likely factors are the deformation mechanisms of antigorite (see discussion). Qualitatively, in situ
329 X-ray diffractions during deformation (not shown) show a lattice preferred orientation for
330 antigorite, with the normals to the basal planes 001 mostly parallel to the maximum compression
331 direction. This texture is stronger at the end of the deformation.

332 The EBSD data on olivine were analysed using the Matlab MTEX toolbox (Bachmann et
333 al., 2010). Fig. 5 shows the pole figures in the two-phase aggregates compared with pole figures
334 for their respective reference aggregate with 100% olivine (pbnm setting).

335

336

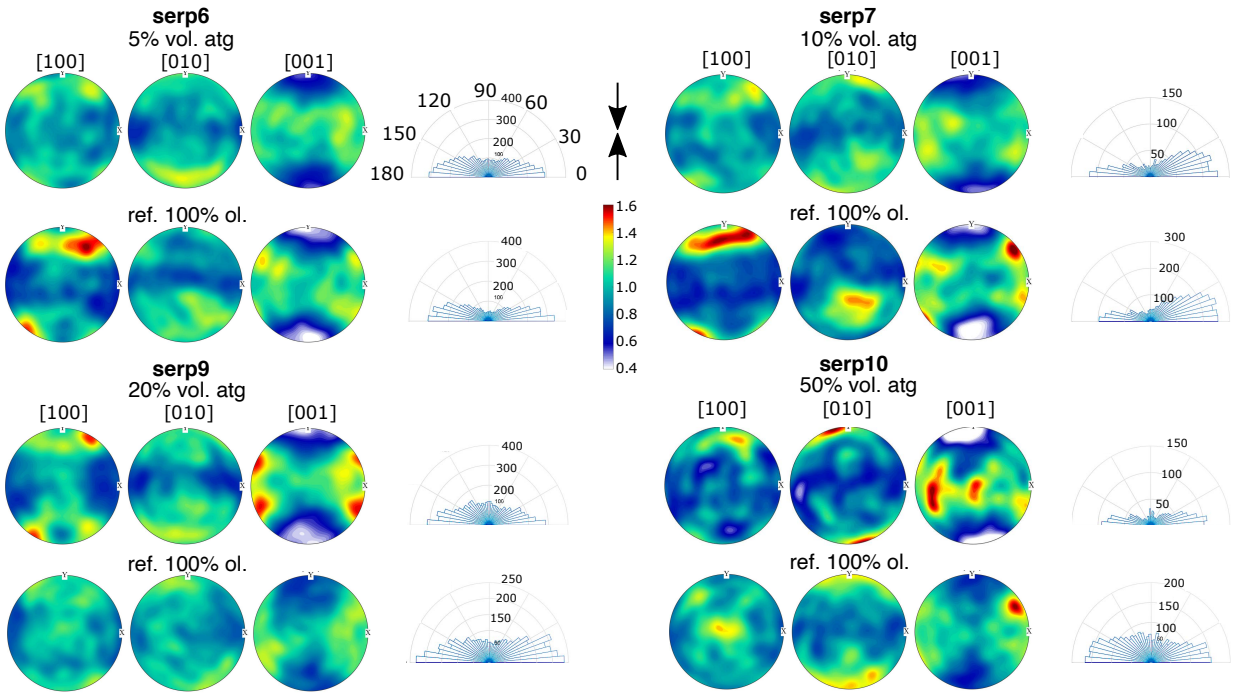

Figure 5. Olivine pole figures and grains long axis orientations in two-phase and reference aggregates, relative to the maximum compression direction, as obtained from EBSD on recovered samples. Color scale bar in mrd (multiples of random deviation); the maximum compression axis is vertical, indicated by the black arrows (90° on the rose diagrams).

The Crystal Preferred Orientations (CPO) on deformed samples are overall weak and are characterized by minima of [001] parallel to the maximum compression direction. The [100] axes define maxima slightly tilted from the maximum compression direction (or weak girdles around this direction). The [010] distribution relative to the maximum compression axis is more diffuse except on the serp10 sample. All two-phase samples showing maximum close to the compression direction.

To deconvolute the final CPO from the one resulting from the loading stage, the lattice preferred orientation (LPO) prior deformation have been analysed for two-phase aggregates using their in situ X-ray diffractions, under high pressure and high temperature (see figure S4 and text). Comparison with the starting textures shows that deformation induced, in all two-phase samples, rotation of the b axes and a axes closer to the maximum compression direction.

In order to characterise the strength of the CPO we use the J-index (Bunge, 1982), which is 1 for a uniform distribution and infinite for a single orientation. The J-index for all samples is shown in figure S5. Overall, the CPO intensity sligthly increases with increasing total strain from

1.07 for the lowest strains to 1.22 for the highest antigorite fraction (50%) and large strain (-23.6%) in the two-phase aggregates. The reference olivine aggregates also show a trend with low J-index of 1.06, for the lowest strains (-12.9%), up to a J-index of 1.2 for the highest strains (-23.6%).

The crystal long axis orientations relative to the compression axis are shown on rose diagrams in fig. 5 for the two-phase and reference aggregates. This long axis is mostly oriented normal to the compression axis, which evidences a Shape Preferred Orientation (SPO).

The local misorientation within olivine grains gives information on the global strain gradient in the grain and the spatial distribution of this gradient. The Kernel Average Misorientation (KAM; angle, within a grain, between a pixel orientation and the mean orientation of its 4 neighbours) reveals local strain gradients within the grains while misorientations to the mean grain orientation ("Mis2Mean") reflects the strain gradient at the grain scale. Maps of KAM and Mis2mean highlight deformation styles of olivine that range between brittle to crystal-plastic end-members (fig. 6).

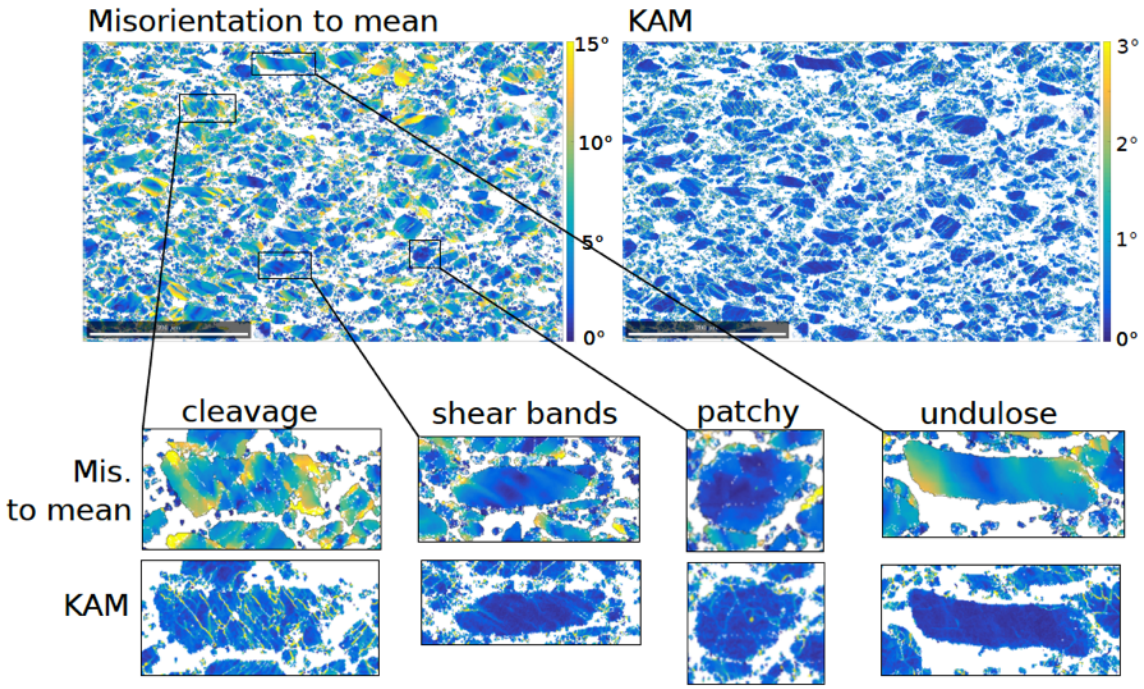

Figure 6. Misorientation to mean grain orientation and kernel average misorientation (KAM) maps on serp9 recovered two-phase aggregate (20 vol. % antigorite). Only olivine was analysed; the white is serpentine and non-indexed regions. The different deformation styles of olivine crystals are highlighted. The scale bar on large maps is 200 µm.

Crystals, especially large ones, show multiple intragranular microcracks, sometimes akin to cleavage. For some, deformation occurs mostly by microcracking and there is only limited misorientation relative to the mean grain orientation. In other cases, the crystals (small or large) show few or no microcracks and undulose to patchy orientation sectors developed within grains. For large grains, KAM maps also highlight a number of impingment microcracks, ie. crack radiating out of the contact sites with other grains (Passchier and Trouw, ed. 2005). Grain microcracks tend to follow diagonal directions, and overall the deformation style is rather cataclastic. We also obtained inverse pole figures showing the rotation axis orientation for low-angle boundaries (2-10°) which are presented in the supplementary material (fig. S6).

4 Discussion

4.1 Deformation mechanisms

4.1.1 Antigorite

The loss of definition of the antigorite peaks on the X-ray diffraction as deformation proceeded, especially on the 5 vol. % atg sample, can indicate one or all of the following processes in this sample: delamination, grain size reduction (comminution), loss of order in the layers stack, large scale crystal defects, and/or amorphisation of antigorite crystals. These mechanisms, except for the stacking disorder, can create new weak zones and cause a decrease in measured stress. After about 18% strain, no peak could be seen anymore on the diffraction for the 5 vol. % atg sample.

We were unable to observe antigorite deformation mechanisms using EBSD. The difficulty in obtaining a signal suitable from EBSD was expected for the aggregates with low antigorite content, because the in-situ XRD indicated some state akin to loss of crystal structure ordering or comminution. However, it was unexpected for the aggregates with highest antigorite content. The small grain sizes lead to crystals being very easily scraped off the surface during preparation, which could have prevented obtaining a good enough polish on antigorite grains. Another possibility is a large number of defects or distorsion in antigorite, too large for the crystals to provide an EBSD signal.

4.1.2 Olivine

The analysis for the intracrystalline deformation mechanisms in olivine requires caution. The CPO are very weak, and the effect of dislocation glide is likely convoluted with crystal shape effects, ie. the SPO. The rose diagrams show a clear correlation between crystal shapes and orientations relative to the shortening axis, hence a well-defined SPO (fig. 5). For olivine reference aggregates (serp6 and 7, table 1) the SPO is slightly stronger in the more deformed aggregates. This relationship is not clear for two-phase aggregates (fig. 5).

The CPO of reference aggregates in serp 6, serp7 and 20 vol. % atg aggregate in serp9 have a majority of [100] close to the maximum compression axis and a girdle of [001] perpendicular to the compression axis, which would be consistent with the (100)[001] slip system. The misorientation analysis fig. S6 (supplementary material) gives further information

about the dislocations locally accomodating the plastic deformation of olivine crystals, which are consistent with the suggested slip system.

We examined possible trends of deformation at the crystal scale with respect to the total sample strain, fraction of antigorite, and aggregate stress. Together with the KAM for local misorientation gradients, the grain orientation spread (GOS; average of Mis2Mean for each grain) was considered, which quantifies the global gradient of orientation existing in the grain. Statistics of the KAM and GOS are presented in fig. S7. The reference olivine aggregates tend to show increased median KAM and median GOS (fig. S7), ie., to be more damaged with increasing stress and strain. Meanwhile, in the olivine within the two-phase aggregates, the median GOS shows a slight tendency to decrease with antigorite fraction (or with decreasing stress) even at larger strains.

These observations are consistent with Wallis et al, 2011, who reported natural microstructures for antigorite free and antigorite bearing dunites of ca.1 0, 21 and 42% modal fraction of antigorite, derived from mantle wedge conditions in the Higashi-Akaishi body, NE Japan. They observed weakening of the olivine CPO with increasing antigorite fraction, due to phase boundary slip and rigid rotation of olivine grains.

4.1.3 Deformation mechanisms of the aggregate

The SEM observations, CPO and SPO all point to 1) intracrystalline plasticity in olivine, which gradually generates the crystal lattice bending and undulose or patchy orientation domains in crystals, for accomodating local strain incompatibilities, and 2) a shortening mainly accomodated by crushing/cleaving of crystals, and by rigid rotation of olivine crystals according to their shape.

The rigid rotations imply grain boundary slip in olivine or between olivine and antigorite in a diffusionless sense (at this experimental timescale, because T is low and in the absence of fluid). Olivine crystal rotation can also be purely accomodated by strain in neigbouring antigorite, in the samples with higher antigorite fractions (e.g. serp10, Figure 3h).

The deformation style of antigorite clusters evolves with increasing antigorite fraction and is consistent with the stress analysis : the low stress in antigorite, for low antigorite fractions (serp6 and 7) is due to the olivine matrix controlling the strain. Hence, antigorite clusters in this

441 case (figures 3b and d) are weakly deformed. At 20 vol. % antigorite, the strain is no longer
442 controlled by olivine only, and the antigorite clusters are sheared (figure 3f). The antigorite
443 clusters have maximum length scales around 200 microns and more typically are about 100
444 microns, and therefore are not connected in 2D over the aggregate length scale. We propose that
445 the en-echelon organization of these clusters forms a weak zone in the aggregate at the scale of
446 the group, even if the clusters are not connected. As proposed for instance by Gerbi et al., (2016),
447 fine-grained olivine can form bridges between antigorite clusters and could also constitute weak
448 zones (not obvious on our 2D images). More likely here, glide on bridging grain boundaries
449 could also play a similar role.

450 The semi-brittle/brittle components of the aggregates' deformation in our experiments are
451 further examined in the light of the available literature in section 4.3.

452 4.2 *In situ* stresses from X-ray data and interpretation

453 Figure 7 compares the stresses within olivine and antigorite in the aggregates as a
454 function of the serpentine fraction in the two-phase aggregate. The stress in the reference
455 aggregate of each run is also reported.

456 Run serp9 showed macroscopic fracturing and a jump in strain for the olivine reference
457 aggregate so comparison of its microstresses with the other runs presented here deserves to be
458 justified. The stress curves in serp9 do not indicate a stress drop simultaneously with the strain
459 jump. In previous works where high-pressure failure took place (e.g., Ferrand et al., 2017; Incel
460 et al., 2017), the stress was measured on a small portion of the sample (200 x 200 μm for a 3 x 2
461 mm sample). In contrast, here the stress was measured on a larger sample area (ca. 1 mm wide x
462 0.5 mm height) centered over ca. 1.3 mm height aggregates, which means we were less likely to
463 miss a major stress drop in the fractured region. We infer that fracturation is only evidenced in
464 the strain data because the volume of crystals in which stress was « unloaded » by this
465 fracturation remained small. Thus, we also consider the stress balance betwen the two phases in
466 this experiment can be compared with our three other experiments.

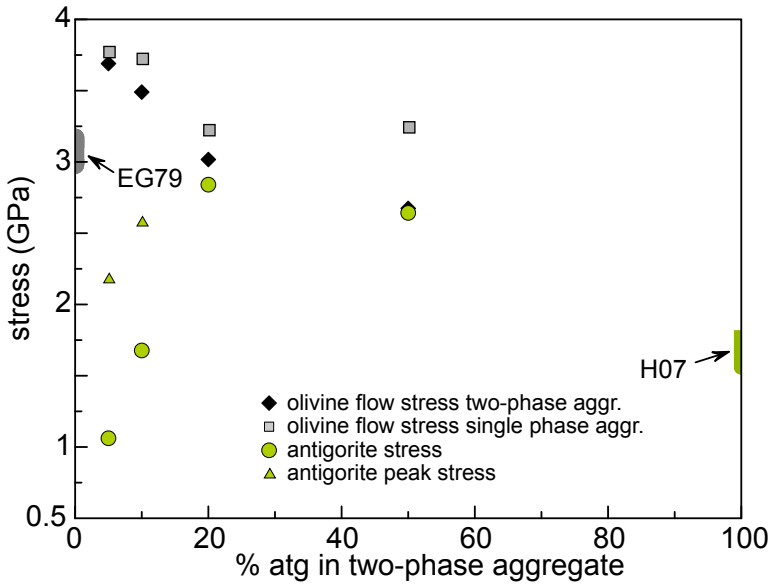

Figure 7. Stresses measured within olivine and antigorite in two-phase aggregates. The stresses for olivine (black) and for antigorite (green) are taken when the stresses have reached a « plateau » on the stress-strain curve (Table 1). For antigorite, the stress is measured only on the (001) plane, see discussion for its significance; the peak stress before the plateau, if any, is indicated by a light green triangle. Stresses in olivine reference aggregates (same run) are in grey. The range of expected stresses under the strain rate, T and P of the four experiments using flow laws by Evans and Goetze (1979) [EG79] and Hilairet et al. (2007) [H07] were calculated for single phase olivine and antigorite aggregates respectively. Note these experimental stresses are not normalized to same strain rate, pressure and temperature. Doing so has a modest effect on stress values and does not change the conclusions here.

In antigorite-poor aggregates (5 and 10 vol. %), the antigorite stress first increases above the stress expected for deformation of pure antigorite aggregates. The olivine framework imposes this transient overshoot in stress, since the overshoot is not observed in pure antigorite aggregates (e.g. Hilairet et al., 2007, Hirauchi et al., 2020). We postulate the antigorite is confined within the olivine matrix and first undergoes elastic compression leading to the peak in stress, because unable to deform freely (strain incompatibilities). After the transient, for 5 vol. % antigorite, the stress decreases below that expected for a pure antigorite aggregate. At that time, the stress in antigorite crystals could be shielded by olivine. Alternatively these low stresses could be due to deformation of very fine grained or partly amorphized antigorite. In the 10 vol. % antigorite aggregate, the stress given by antigorite after the transient stage is consistent with the flow stress expected for a pure antigorite aggregate. Thus the local strain rate imposed to the

antigorite patches may be close to that of the aggregate at this time. The deformation at the aggregate scale is buffered by the stress percolating within the framework of olivine crystals.

For the 20 and 50 vol. % antigorite aggregates, the stress balance is different from that with lower atg fraction. No transient regime is observed. Antigorite indicates higher stresses than expected from its flow law in these P, T and strain rate conditions, and similar to those of olivine (fig. 7). The explanation can reside in microstructural factors and/or come from different deformation mechanisms than those corresponding to the flow law in Hilairet et al (2007). As for microstructural factors: with a weak CPO and five measured diffraction planes (which thus cover many different orientations in the olivine unit cell), the olivine stress is calculated from a population of diffracting grains that sample a large orientation range. The situation is quite different for serpentine, which becomes strongly textured in our experiments. The population of diffracting grains for the only measured diffraction plane (the basal plane (001)) is in vast majority made of grains oriented orthogonal to the beam when the stress plateau is reached. If deformation can occur in antigorite by a mechanism (as yet unclear), which end-result is glide more or less parallel to the (001) planes, most grains oriented perpendicular to the maximum stress direction are therefore not able to accomodate deformation anymore. Amiguet et al. (2012) investigated lizardite aggregate deformation, and referred to such population as having a « locked geometry ». Our lattice strain Q(001) is calculated from a full angular dispersive diffraction line, and therefore includes grains in « unlocked » orientations. However, the stronger the texture, the less unlocked grains can contribute, and the higher may become the influence of the locked grains on the stress as calculated from the lattice strains *Q(hkl)*. Thus, for our 20 and 50 vol. % antigorite samples, these locked grains are in an isostress state with the olivine crystals. The second factor that can explain this discrepancy is a mix of deformation mechanisms that are different than those occurring in Hilairet et al. (2007), specifically a larger part of brittle like mechanisms. This is examined in the next section.

4.3 Comparison with antigorite and olivine deformation experiments from the literature.

In our experiments the deformation mechanisms are more akin to frictional processes *sensu lato* (diffusionless sliding on grain boundaries and cracks, microcracking and delamination) than purely (intra)crystalline defects-controlled processes, because of the high strain rates, low temperature, high stress level and the absence of fluids.

From X-ray diffraction, the 'hydrostatic' pressure P (mean stress) and the differential stress σ_d are measured *in situ*. Taking compressive stresses as positive, σ_1 and σ_3 as the maximum and the minimum compressive stress respectively, assuming the transversal isotropy of stresses $\sigma_2 = \sigma_3$ because of the cylindrical geometry of the sample and compression, we have $P = \frac{1}{3}(\sigma_1 + 2\sigma_3)$ and $\sigma_d = \sigma_1 - \sigma_3$. Therefore σ_1 and σ_3 are straightforwardly obtained from $\sigma_1 = P + \frac{2}{3}\sigma_d$ and $\sigma_3 = P - \frac{1}{3}\sigma_d$. From this, the state of stress on any given plane within the aggregate can be characterized and plotted as a Mohr circle.

The tangential stress τ on a plane reads:

$$\tau = \frac{1}{2}\sigma_d \sin 2a$$

where α is the angle between the plane normal and the minimum compressive stress (α is used to avoid confusion with θ already defined as the diffraction angle).

The normal stress σ_n reads:

$$\sigma_n = \left(\frac{\sigma_1+\sigma_3}{2}\right) - \left(\frac{\sigma_1-\sigma_3}{2}\right)\cos 2a.$$

Fig. 8a shows this stress state as Mohr-Coulomb circles for pure olivine and two-phase aggregates in this study. For the run serp10, the stress state actually used for the figure in the reference aggregate is taken at 13 % shortening, while for the two-phase aggregate the total strain is above 20%. Since in the latter, the stress does not vary between 13% and 20% strain (fig. 2 lower right) they can still be compared here. For the same reason, the stress states of the other runs are also those at the final strain even if these differ (table 1).

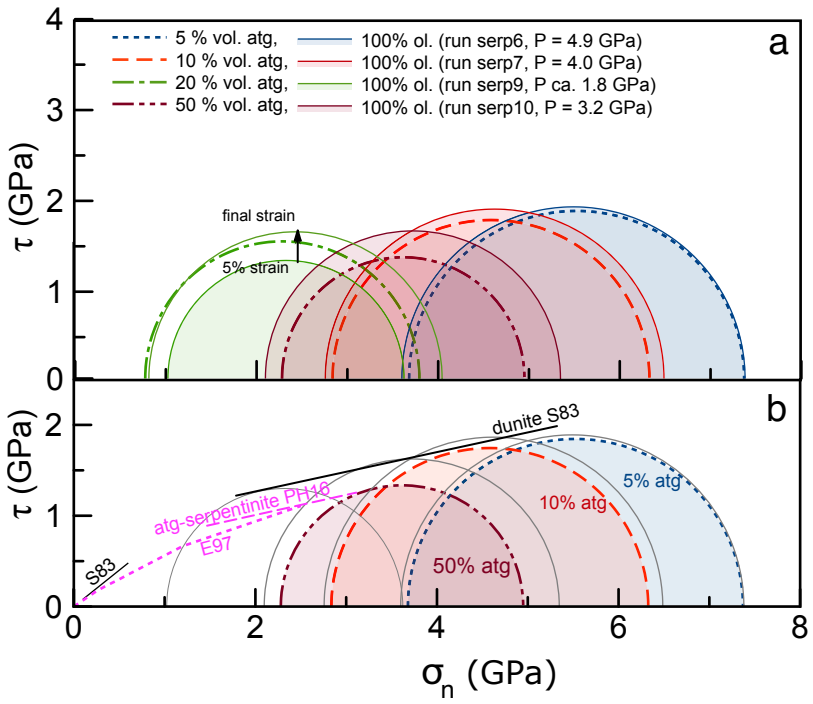

Figure 8. Strength of two-phase aggregates and comparison with friction laws for antigorite and olivine. a) Mohr circles representing the stress state in two-phase and reference single-phase aggregates in this study, as calculated from in-situ measurements of differential stress and pressure (mean stress). The stress values at final strain were considered as representative. For run serp9, stress state on the reference aggregate is plotted at ca. 5% (before strain jump ; cf. fig. 1) and at final strain. b) Data from this study compared with friction laws from literature : Escartin et al., (1997) [E97], Proctor and Hirth (2016) [PH16], for antigorite, and Shimada (1983) [S83] for dunite. Serp9 two-phase aggregate stress state is not reported for clarity (in a), dashed green circle).

In fig. 8b, we compare these data with friction laws and fracture envelopes from the litterature, i.e., the so-called Byerlee law defined by a compilation of rock mechanical data (friction) up to 2 GPa for σ_n (Byerlee, 1978), and the fracture envelope reported for the Horoman dunite by Shimada (1983). The results on olivine aggregates by Boettcher et al. (2007) are not included because less relevant (with fluid, up to 300 MPa effective pressure only, and temperatures from 600°C to 1000°C). For antigorite aggregates, the Mohr envelope obtained by Escartin et al. (1997) and Proctor and Hirth (2016) at higher pressures are shown.

For reference aggregates (100% olivine) in serp6, serp7 and serp10, the stress states on fig. 8 do correspond to the fracture envelope determined on the Horoman dunite by Shimada (1983). For the two-phase aggregates, when antigorite fraction is low (5 vol. % atg), the olivine

554 indicates a state of stress similar to the pure olivine aggregate. Meanwhile, for high antigorite
555 content (50 vol. %), the stress state in olivine is much lower than in the reference, and can be
556 interpreted as buffered by the antigorite frictional properties measured by Escartin et al., (1997)
557 and Proctor and Hirth (2016). In this case, olivine crystals likely behave as rigid inclusions.
558 Antigorite indeed controls the deformation above 20 vol. % antigorite, and mechanisms akin to
559 frictionnal processes, such as those reported at lower pressure, control the stress in antigorite.

560 In run serp9 the state of stress in the reference aggregate at the final strain is above the
561 envelope defined by Shimada et al (1983). When the stress state is taken at 5% strain, where a
562 strain jump occurs (fig. 1) likely due to a sample fracture, the Mohr circle actually fits the
563 fracture envelope by Shimada 1983 (fig. 8, circle marked 5% strain). Further increase in stress
564 may be an indication of the fracture being locked and/or of sample hardening due to
565 intracrystalline defects multiplication. For the antigorite+olivine aggregate in this run the stress
566 state is also well above the fracture envelope for dunite, and the friction law defined for pure
567 antigorite aggregates in Proctor and Hirth (2016) (similar to its reference olivine aggregate). The
568 stress state is however, in this run, measured from the olivine crystals and a subpopulation of
569 antigorite crystals in locked orientations. The actual stress under which the two-phase aggregate
570 deforms (ie. force over surface), may be lower than the one measured in these olivine and
571 antigorite crystals, in the case of deformation localization. The en-echelon organization seen in
572 figure 3e is a candidate region in this sample. Hardening may be invoked in other regions of the
573 sample.

574 Note that Shimada's experiments had a larger grain size (0.1 to 0.9 mm compared to 1-40
575 microns here) and were conducted at ambient T, while our experiments are at 300 to 350°C .
576 Therefore the dependence of fracturation/frictional properties of olivine on grain size or T of
577 aggregates cannot be discussed here. We also provide in fig. S8 a comparison with data available
578 for deformation of olivine or antigorite under low T at similar or higher confining pressures that
579 plot close to or above the Goetze criterion, together with a short discussion.

580 In summary, our data at low temperature are consistent with previously determined
581 friction laws in olivine and antigorite aggregates, and suggest their continuity for T up to ca
582 350°C, even at these high pressures up to 4-5 GPa. Experiments under low temperature below
583 ca. 900 K, and high pressures above ca. 2 GPa, are commonly fitted using an exponential flow

law – which implies a deformation controlled by dislocation glide under high stresses. It is yet unclear to us whether one of these frameworks represents best our data. This calls for a better understanding of how to describe deformation mechanisms within antigorite aggregates, which do not obey simple dislocation glide-based mechanisms (Idrissi et al., 2020, Hansen et al., 2020).

4.4 Antigorite fraction: threshold for changes in mechanical control

The differences in strain rates and in-situ stresses recorded by the 5 and 10 vol. % antigorite aggregates on one side, and the 20 and 50 vol. % antigorite aggregates on the other side, highlight a change in the aggregate mechanical behavior between 10 and 20 vol. % antigorite. This value is also reflected in the change in local olivine crystal plasticity as previously discussed (see olivine deformation mechanisms, section 1.2). This threshold does correspond to the usual values for stress percolation problems of a weak phase within the framework of a stronger phase (e.g., Karato, 2008).

This threshold is somewhat different from that obtained in experiments at ambient T by (Escartin et al., 2001) in which about 5 -10 vol. % lizardite and chrysotile serpentine decreased the overall strength of serpentinized peridotites by a factor of 2-3. This difference is easily explained by the crystallographic structure of antigorite (e.g. Escartin et al., 2001; Amiguet et al., 2012) which is more compact than lizardite. As a result, lizardite (and chrysotile) have internal friction coefficients much lower than antigorite (Escartin et al., 1997). A second explanation resides in the microstructure : while our samples are synthetic aggregates with patches or grains of antigorite within a matrix of olivine, the rock used by Escartin et al. (2001) was a peridotite in which former olivine grain boundaries were lined up by lizardite and chrysotile, interconnected despite a low volume content. As proposed by Handy (1990), this comparison illustrates that microstructure is crucial in controlling and modifying the mechanical behavior of an aggregate even at modest strains.

Ferrand et al. (2017) and Ferrand (2017) used the same starting material than in this study, with varying antigorite contents (0, 5, 20 and 50 vol. %) for investigation of the link between intermediate-depth earthquakes and serpentine dehydration, in similar conditions of strain, pressure, similar microstructure, and higher temperature (ca. 500°C) and strain rates (5.10^{-5} to 10^{-4} s^{-1}). In Ferrand et al. (2017), aggregates containing as little as 5 vol. % antigorite showed already lower olivine stresses than pure olivine aggregates in the same conditions, suggesting

that temperature or strain rate modify the elastic and crystal-plastic interactions between olivine and antigorite.

Given the microstructural observations, the single-crystal strength of olivine is expected to have a major role in controlling deformation of the reference aggregates or antigorite-poor aggregates. However, the stresses obtained for the 100% olivine reference aggregate and two-phase aggregates at the highest pressures, are higher than single-crystal hardness measured by Evans and Goetze (1979) using an indentation technique. Those at lower pressures are consistent with Evans and Goetze (1979). The higher stresses seen in the highest pressure experiments thus could be due to the pressure effect on the deformation mechanisms, not taken into account in the flow law by Evans and Goetze (1979).

In addition to these pressures differences, the strain rates at which the single-phase aggregates and two-phase aggregates deform here differ, up to a factor of almost 4. We attempt here to make a comparison "free" from strain rate and pressures variations~~, and compare with the literature,~~ by defining for the two-phase and reference aggregates in each experiment :

$$\eta_{two\ phase} = \frac{\sigma_{two\ phase}}{\dot{\varepsilon}_{two\ phase}} \text{ and } \eta_{ref} = \frac{\sigma_{ref}}{\dot{\varepsilon}_{ref}} \ .$$

Figure 9 shows the evolution of the ratio $\frac{\eta_{two\ phase}}{\eta_{ref}}$ as a function of antigorite content, and a comparison with literature data. Studies at higher temperatures are not included for the sake of clarity, but can be found in Ferrand (2017). Contrasts expected for monomineralic antigorite or lizardite (chrysotile) rocks with respect to dunite, are calculated from published flow laws (Hilairet et al., 2007, Amiguet et al., 2012, Evans and Goetze, 1979). The flow laws calculated contrasts are consistent with the shear strain contrasts between pure antigorite, lizardite (chrysotile) and olivine aggregates found by Hirauchi and Katayama (2013) at 300°C under 1 GPa confining pressure. Note the use of these flow laws for pure end members implies a deformation by dislocation-motion controlled processes, while our data seem (also) consistent with friction-like controlled behavior.

At moderate temperatures, our aggregate with 5 vol. % antigorite has a higher $\frac{\sigma}{\dot{\varepsilon}}$ than its single-phase counterpart in the same run, with similar stresses in both aggregates. The lower strain rate of the two-phase aggregate is what causes this apparent higher "viscosity", and could be interpreted as a result of local hardening of olivine at low serpentine fractions. Handy (1990)

for instance (his fig. 1) suggest a hardening effect at low amounts of weak phase in such aggregates. Comparing with Ferrand et al (2017), we infer this hardening vanishes closer to dehydration temperatures because intracrystalline deformation processes are more active. Figure 9 is further discussed in the next section.

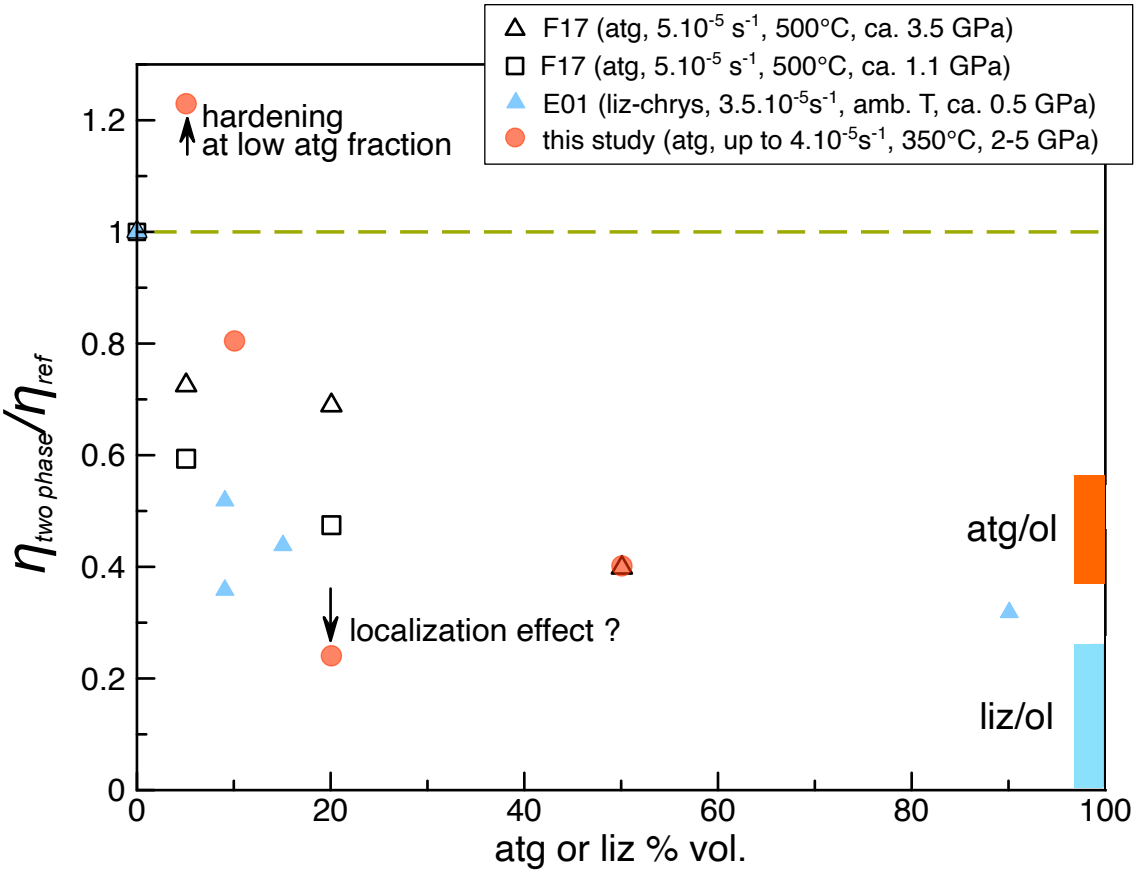

Figure 9. Contrast in $\eta = \frac{\sigma}{\dot{\varepsilon}}$ between serpentine+olivine aggregates and pure olivine aggregates, from this study and the literature. The aggregate strengths in this study are normalized by the strain rates (all different from one aggregate to another), the two phase aggregates compared against the reference aggregate for each run. Data from Ferrand et al, 2017 (F17) were normalized using their 100% olivine aggregates runs at 3.5 and 1.1 GPa. Lizardite-serpentinites data from Escartin et al, 2001 (E01) were normalized using their unaltered Horoman Dunite data with the pressure (mean stress) calculated from the confining pressure (σ_3) and the differential stress. The contrast for antigorite or lizardite rocks compared to dunite ([atg/ol] and [liz/ol] respectively) is calculated from published flow laws which implies theoretically deformation controlled by dislocation motion processes. Hilairet et al, (2007) is used for antigorite, Amiguet et al, (2012) for lizardite, and Evans and Goetze (1979) for olivine with strain rate 2.10^{-5} s^{-1}, P between 1 and 3 GPa, T at 400°C. See sections 4.4 and 4.5 for discussion.

4.5 Applicability to subduction zone dynamics

Our aggregates with varied antigorite contents can be considered as a proxy for dunite with different serpentinization degrees, and our olivine aggregates as a proxy for a mantle unaltered dunite. Fig. 9 thus shows estimates of the strength or viscosity contrast between these two rocks at our experimental strain rates, ie., for timescales ranging from hours to days.

At high pressures corresponding to depths of 90 km, our results suggest the viscosity could be inverted at very low serpentine (5%) fractions because of the local concentration of stresses. The viscosity contrast could remain on the order of 0.7 or higher for a serpentine amount of 10 vol. %, and around 0.4 to 0.5 for 50% serpentinization or more. The viscosity contrast for 20 vol. % antigorite, lower than 0.3, may be due to the proposed strain localization along the en-echelon antigorite clusters. Further experiments would be needed to clarify the role of mean stress here.

The viscosity contrast becomes larger for a lower serpentine amount, in the lower pressure, higher temperature series in the antigorite-bearing samples in Ferrand et al. (2017, 1.1 GPa series), and for the lizardite-chrysotile serpentinites deformed under a mean stress ca. 0.5 GPa and at ambient T in Escartin et al., (2001). The difference between our results and those of Ferrand et al. (2017) at low antigorite contents, is likely the balance of controlling deformation mechanisms for olivine. Frictional processes *s.l.* occur in our experiments at low T, while intracrystalline olivine plasticity can be expected more active at higher T ~~in Ferrand et al. (2017)~~ (e.g. results by Raterron et al, 2004). This may however be mitigated by an increased strain rate.

For a large serpentine content (50% and more) at first order the strength contrast between a serpentinized rock and an olivine rock does not seem to depend on the T or the mix in deformation mechanisms (brittle-like vs. intracrystalline): this contast is similar and around 0.4 to 0.5, whether it is taken at high T (Ferrand et al. 2017), in our aggregates at lower T, or if calculated from a flow law in a pure antigorite rock with a different mix of these deformation mechanisms.

The hardening of the aggregate with the lowest serpentine fraction (5%) relative to pure olivine aggregate, and the shielding of stress within antigorite for 5 and 10 vol. % serpentine aggregates, can be related to the creation of load-bearing networks (e.g. Handy, 1990, 1994) or force chains (a concept widely known in granular mechanics, e.g. Peters et al., 2005) through the

harder olivine grains, in contact with each other. The relevance of this hardening for a natural serpentinized peridotite and for different microstructures remains to be demonstrated. Recently, Burnley (2013), and Beall, Fagereng and Ellis (2019a, b), studied numerically the development of force chains in deforming aggregates, and shear zones at cm to m scale, respectively. These studies, the results by Ferrand et al., (2017) on dehydrating antigorite+olivine aggregates, Ferrand (2019), and the present study, suggest that when the weak component is between 0 and 20 vol. %, understanding the modalities of load-bearing networks appearance, and characterizing them at several scales, is essential in describing the rheology of polymineralic and matrix/clast mélanges.

Our dataset remains limited, with several parameters at play that have opposite effects (temperature, pressure, strain rate, plastic properties of crystals, and microstructure). Extrapolation to the natural context and background strain rates must be made with caution. First, the displacement and stress geometry on shear zones, and the resulting microstructure, may be best represented by simple shear experiments. Lower strain rates may lead to different plastic relaxation interactions between antigorite and olivine. Fluids circulate at least episodically in shear zones, in subduction settings, and these fluids promote very different deformation mechanisms in serpentinites such as pressure solution (e.g., Auzende et al., 2015), especially when considering long timescales.

The results here, nonetheless, provide clues on the stress distribution in, and strength contrasts between, rocks when subject to relatively high stresses and high strain rates which may arise in subduction zones. They could be relevant to ductile deformation of serpentinized zones (or shear zones reactivation) upon stress transfer from loaded parts of the subduction zones (e.g. models by Montesi and Hirth, 2003, Regenauer-Lieb and Yuen, 2008, Montesi, 2013, Goswami and Barbot, 2018, observations by Hirauchi et al., 2021), where high stresses/fast strain rates may transiently be achieved, and to events that occur on timescales of hours to days, such as slow slip events. Because carried out under high pressures (> GPa) and at a temperature close to 350°C, our results could be particularly relevant for the rheology of the so-called stable sliding zone of the interface between the slab and mantle, for the transition between stable sliding and seismic zones, and for understanding the stress state(s) within cold subducting slabs.

Acknowledgments

We thank Ken-ichi Hirauchi, an anonymous reviewer and the Associate Editor for their comments that helped improve a previous version of this manuscript, and Keishi Okazaki and Sando Sawa for their reviews. The experiments were performed on the ID06-LVP beamline at the European Synchrotron Radiation Facility (ESRF), Grenoble, France. The EBSD part of the electron microscopy was performed at the EBSD facility at Geosciences Montpellier, a national facility of CNRS-INSU (Institut National pour les Sciences de l'Univers). The remaining SEM images were obtained at the PMEL facility in Lille (France), supported by the Conseil Régional du Nord-Pas de Calais, and the European Regional Development Fund (ERDF). We thank F. Barou and C. Nevado (U. Montpellier) for assistance with the EBSD measurements and samples polishing. N.H. and S.M. acknowledge the Institut Chevreul for help in the development of this work (facility funding) through the ARCHI-CM project supported by the "Ministère de l'Enseignement Supérieur de la Recherche et de l'Innovation", the region "Hauts-de-France", the ERDF program of the European Union and the "Métropole Européenne de Lille". T. P. F. was supported by the ANR projet DELF to A. Schubnel (ANR12-JS06-0003) early in this work, and by the *Alexander von Humboldt* Foundation (TPF grant). P. R. research activities were in part carried out while P. R. was serving at the National Science Foundation (NSF). This study was initiated thanks to the financial support of the INSU Programme National de Planétologie to N.H. and P.R., and funded by the Agence Nationale pour la Recherche (MADISON, ANR-17-CE31-0012-01 to N.H.).

Open Research

Availability statement: The stress and strain data from this study are available in a .csv text file, at the https://www.data.gouv.fr/fr/ repository via the link xxxx, and the persistent identifier is the following doi : xxxxx.

References

Abers, G. A., van Keken, P. E., Kneller, E. A., Ferris, A., Stachnik, J. C. (2006) The thermal structure of subduction zones constrained by seismic imaging: Implications for slab dehydration and wedge flow, *Earth and Planetary Science Letters, 241*, 3–4, 387-397, 10.1016/j.epsl.2005.11.055.

Abers, G.A., Nakajima, J., van Keken, P.E., Kita, S., Hacker, B.R. (2013) Thermal-petrological controls on the location of earthquakes within subducting plates, *Earth and Planetary Science Letters 369*, 178-187, doi: 10.1016/j.epsl.2013.03.022

Agard, P., Plunder, A., Angiboust, S., Bonnet, G., Ruh, J. (2018). The subduction plate interface: rock record and mechanical coupling (from long to short timescales). *Lithos 320*, 537-566, doi: 10.1016/j.lithos.2018.09.029.

Amiguet, E., Reynard, B., Caracas, R., Van de Moortele, B., Hilairet, N., Wang, Y.B. (2012). Creep of phyllosilicates at the onset of plate tectonics. *Earth and Planetary Science Letters 345*, 142-150, doi: 10.1016/j.epsl.2012.06.033.

Auzende, A.L., Escartin, J., Walte, N.P., Guillot, S., Hirth, G., Frost, D.J. (2015). Deformation mechanisms of antigorite serpentinite at subduction zone conditions determined from experimentally and naturally deformed rocks. *Earth and Planetary Science Letters 411*, 229-240, doi: 10.1016/j.epsl.2014.11.053.

Bachmann, F., Hielscher, R., Schaeben, H., 2010. Texture Analysis with MTEX - Free and Open Source Software Toolbox, in: Klein, H., Schwarzer, R.A. (Eds.), *Texture and Anisotropy of Polycrystals III.* doi: 10.4028/www.scientific.net/SSP.160.63

Beall, A., Fagereng, Å., & Ellis, S. (2019a). Fracture and weakening of jammed subduction shear zones, leading to the generation of slow slip events. *Geochemistry, Geophysics, Geosystems, 20*. doi: 10.1029/2019GC008481

Beall, A., Fagereng, Å., & Ellis, S. (2019b). Strength of strained two-phase mixtures: Application to rapid creep and stress amplification in subduction zone mélange. *Geophysical Research Letters, 46,* 169–178, doi: 10.1029/2018GL081252

Bezacier, L., Reynard, B., Bass, J.D., Sanchez-Valle, C., Van de Moortele, B. (2010). Elasticity of antigorite, seismic detection of serpentinites, and anisotropy in subduction zones. *Earth and Planetary Science Letters 289*, 198-208, doi: 10.1016/j.epsl.2009.11.009.

Boettcher, M.S., Hirth, G., Evans, B., 2007. Olivine friction at the base of oceanic seismogenic zones. *Journal of Geophysical Research-Solid Earth 112*, doi: 10.1029/2006jb004301.

Bunge, H.J. (1982). *Texture Analysis in Material Sciences: Mathematical methods.*

Burdette, E., & Hirth, G. (2022). Creep rheology of Antigorite: Experiments at subduction zone conditions. *Journal of Geophysical Research: Solid Earth*, *127*, e2022JB024260. doi: 10.1029/2022JB024260

Burnley, P.C. (2015). Elastic plastic self-consistent (EPSC) modeling of plastic deformation in fayalite olivine. *American Mineralogist 100*, 1424-1433, doi: 10.2138/am-2015-5234CCBYNCND

Burnley, P.C., Zhang, D. (2008). Interpreting in situ x-ray diffraction data from high pressure deformation experiments using elastic-plastic self-consistent models: an example using quartz. *Journal Of Physics-Condensed Matter 20,* 285201, doi: 10.1088/0953-8984/20/28/285201

Burnley, P. C. (2013) The importance of stress percolation patterns in rocks and other polycrystalline materials, *Nature Communications 4*, doi: 10.1038/ncomms3117

786 Byerlee, J. (1978). Friction of rocks. *Pure and applied geophysics 116*, 615-626, doi:
787 10.1007/BF00876528.

788 Canova, G.R., Wenk, H.R., Molinari, A. (1992). Deformation modeling of mutliphase
789 polycrystals - case of a quartz mica aggregate. *Acta Metallurgica Et Materialia 40*, 1519-
790 1530, doi: 10.1016/0956-7151(92)90095-v

791 Chen, J.H., Li, L., Yu, T., Long, H.B., Weidner, D., Wang, L.P., Vaughan, M. (2006). Do Reuss
792 and Voigt bounds really bound in high-pressure rheology experiments? *Journal of*
793 *Physics-Condensed Matter 18*, S1049-S1059, doi: 10.1088/0953-8984/18/25/s11.

794 Chernak, L.J., Hirth, G. (2010). Deformation of antigorite serpentinite at high temperature and
795 pressure. *Earth and Planetary Science Letters 296*, 23-33, doi:
796 10.1016/j.epsl.2010.04.035.

797 Chernak, L.J., Hirth, G. (2011). Syndeformational antigorite dehydration produces stable fault
798 slip, *Geology 39* (9), 847-850, doi:10.1130/G31919.1

799 Cook, A. C., Vel, S. S., Gerbi, C., and Johnson, S.E. (2014), Computational analysis of nonlinear
800 creep of polyphase aggregates: Influence of phase morphology, *Journal of Geophysical*
801 *Research-Solid Earth, 119*, 6877–6906, doi:10.1002/2014JB011197.

802 Cyprych, D., Brune, S., Piazolo, S., Quinteros, J. (2016). Strain localization in polycrystalline
803 material with second phase particles: Numerical modeling with application to ice
804 mixtures. *Geochemistry Geophysics Geosystems 17*, 3608-3628, doi:
805 10.1002/2016gc006471.

806 Druiventak, A., Trepmann, C.A., Renner, J., Hanke, K. (2011). Low-temperature plasticity of
807 olivine during high stress deformation of peridotite at lithospheric conditions — An
808 experimental study. *Earth and Planetary Science Letters 311*, 199-211, doi:
809 https://doi.org/10.1016/j.epsl.2011.09.022.

810 Dobson, D. P., P. G. Meredith, and S. A. Boon (2002), Simulation of subduction zone seismicity
811 by dehydration of serpentine, *Science 298* (5597), 1407-1410, doi:
812 10.1126/science.1075390

813 Escartin, J., Hirth, G., Evans, B. (1997). Nondilatant brittle deformation of serpentinites:
814 Implications for Mohr-Coulomb theory and the strength of faults. *Journal of Geophysical*
815 *Research-Solid Earth 102*, 2897-2913, doi: 10.1029/96jb02792.

816 Escartin, J., Hirth, G., Evans, B. (2001). Strength of slightly serpentinized peridotites:
817 Implications for the tectonics of oceanic lithosphere. *Geology 29*, 1023-1026, doi:
818 10.1130/0091-7613

819 Evans, B., Goetze, C. (1979). Temperature variation of hardness of olivine and its implication for
820 polycryscalline yield stress. *Journal of Geophysical Research 84*, 5505-5524, doi:
821 10.1029/JB084iB10p05505.

822 Evans, B.W. (2004). The serpentinite multisystem revisited: Chrysotile is metastable.
823 *International Geology Review 46,* 479-506, doi: 10.2747/0020-6814.46.6.479.

824 Farla, R., Rosenthal, A., Bollinger, C., Petitgirard, S., Guignard, J., Miyajima, N., Kawazoe, T.,
825 Crichton, W.A., Frost, D.J. (2017). High-pressure, high-temperature deformation of

826 dunite, eclogite, clinopyroxenite and garnetite using in situ X-ray diffraction. *Earth and*
827 *Planetary Science Letters 473*, 291-302, doi: 10.1016/j.epsl.2017.06.019.

828 Federico, L., Crispini, L., Scambelluri, M., Capponi, G. (2007) Ophiolite mélange zone records
829 exhumation in a fossil subduction channel. *Geology 35* (6): 499–502. doi: https://doi-
830 org.insu.bib.cnrs.fr/10.1130/G23190A.1

831 Ferrand, T. P. (2017). *Reproduction expérimentale d'analogues de séismes mantelliques par*
832 *déshydratation de l'antigorite & Comparaison à des pseudotachylites naturelles*
833 *(doctoral dissertation)* PSL★ Research University, Paris, France. https://tel.archives-
834 ouvertes.fr/tel-01559226

835 Ferrand, T. P., Hilairet, N., Incel, S., Deldicque, D., Labrousse, L., Gasc, J., Renner, J., Wang,
836 Y., Green, H.W., Schubnel, A. (2017). Dehydration-driven stress transfer triggers
837 intermediate-depth earthquakes. *Nature Communications,* doi: 10.1038/ncomms15247.

838 Ferrand, T. P. (2019). Seismicity and mineral destabilizations in the subducting mantle up to 6
839 GPa, 200 km depth. *Lithos 334*, 205-230, doi: 10.1016/j.lithos.2019.03.014

840 Gaboriaud, R.J., Darot, M., Gueguen, Y., Woirgard, J. (1981). Dislocations in olivine indented at
841 low temperatures, *Physics and Chemistry of Minerals 7*, 100-104, doi:
842 10.1007/bf00309460.

843 Gasc, J., Schubnel, A., Brunet, F., Guillon, S., Mueller, H-J., Lathe, C. (2011). Simultaneous
844 acoustic emissions monitoring and synchrotron x-ray diffraction at high pressure and
845 temperature: calibration and application to serpentinite dehydration, *Physics of the Earth*
846 *and Planetary Interiors 198* (3-4), 121-133, doi: 10.1016/j.pepi.2011.08.003

847 Gasc, J., Hilairet, N., Yu, T., Ferrand, T., Schubnel, A., Wang, Y. (2017). Faulting of natural
848 serpentinite: Implications for intermediate-depth seismicity, *Earth and Planetary Science*
849 *Letters 474*, 138-147, doi: 10.1016/j.epsl.2017.06.016

850 Gerbi, C., S. E. Johnson, D. Shulman, and K. Klepeis (2016), Influence of microscale weak
851 zones on bulk strength, *Geochem. Geophys. Geosyst., 17,* 4064–4077,
852 doi:10.1002/2016GC006551.

853 Girard, J., Amulele, G., Farla, R., Mohiuddin, A., Karato, S.-i. (2016). Shear deformation of
854 bridgmanite and magnesiowustite aggregates at lower mantle conditions. *Science 351*,
855 144-147, doi: 10.1126/science.aad3113.

856 Guignard, J., Crichton, W.A. (2015). The large volume press facility at ID06 beamline of the
857 European synchrotron radiation facility as a High Pressure-High Temperature
858 deformation apparatus. *Review of Scientific Instruments 86*, doi: 10.1063/1.4928151.

859 Guillot, S., Schwartz, S., Reynard, B., Agard, P., Prigent, C. (2015). Tectonic significance of
860 serpentinites. *Tectonophysics 646*, 1-19, doi: 10.1016/j.tecto.2015.01.020.

861 Goswami, A., Barbot, S. (2018) Slow-slip events in semi-brittle serpentinite fault
862 zones. *Scientific Reports 8*, 6181, doi: 10.1038/s41598-018-24637-z

863 Guyot, F., Wang, Y.B., Gillet, P., Ricard, Y. (1996). Quasi-harmonic computations of
864 thermodynamic parameters of olivines at high-pressure and high-temperature. A
865 comparison with experiment data. *Physics of the Earth and Planetary Interiors 98*, 17-29,
866 doi: 10.1016/S0031-9201(96)03174-3

867 Hammersley, A.P. (2016). FIT2D: a multi-purpose data reduction, analysis and visualization
868 program. *Journal of Applied Crystallography 49*, 646-652, doi:
869 10.1107/s1600576716000455.

870 Handy, M.R. (1990). The solid-state flow of polymineralic rocks. *Journal of Geophysical*
871 *Research-Solid Earth and Planets 95*, 8647-8661, doi: 10.1029/JB095iB06p08647.

872 Handy, M.R. (1994). Flow laws for rocks containing 2 non-linear viscous phases - a
873 phenomenological approach *Journal of Structural Geology 16*, 1727-1727, doi:
874 10.1029/JB095iB06p08647

875 Hansen, L.N., David, E.C., Brantut, N., Wallis, D. (2020). Insight into the microphysics of
876 antigorite deformation from spherical nanoindentation. *Philosophical Transactions of the*
877 *Royal Society a-Mathematical Physical and Engineering Sciences 378*, doi:
878 10.1098/rsta.2019.0197.

879 Hilairet, N., Reynard, B., Wang, Y.B., Daniel, I., Merkel, S., Nishiyama, N., Petitgirard, S.,
880 (2007). High-pressure creep of serpentine, interseismic deformation, and initiation of
881 subduction. *Science 318*, 1910-1913, doi: 10.1126/science.1148494.

882 Hilairet, N., Wang, Y., Sanehira, T., Merkel, S., Mei, S. (2011). Deformation of olivine under
883 mantle conditions: an in-situ high-pressure, high-temperature study using monochromatic
884 synchrotron radiation. *Journal of Geophysical Research 117*, B01203, doi:
885 10.1029/2011JB008498.

886 Hirauchi, K.I., and Katayama, I. (2013) Rheological contrast between serpentine species and
887 implications for slab-mantle wedge decoupling. *Tectonophyics 608*, 545-551, doi:
888 10.1016/j.tecto.2013.08.027

889 Hirauchi, K.I., Katayama, I., Kouketsu, Y. (2020). Semi-brittle deformation of antigorite
890 serpentinite under forearc mantle wedge conditions. *Journal of Structural Geology 140*,
891 104151, doi : 10.1016/j.jsg.2020.104151.

892 Hirauchi, K.-I., Nagata, Y., Kataoka, K., Oyanagi, R., Okamoto, A., Michibayashi, K. (2021)
893 Cataclastic and crystal-plastic deformation in shallow mantle-wedge serpentinite
894 controlled by cyclic changes in pore fluid pressures, *Earth and Planetary Science Letters*
895 *576*, 117232, doi: 10.1016/j.epsl.2021.117232

896 Idrissi, H., Samaee, V., Lumbeeck, G., van der Werf, T., Pardoen, T., Schryvers, D., Cordier, P.
897 (2020). In Situ Quantitative Tensile Testing of Antigorite in a Transmission Electron
898 Microscope. *Journal of Geophysical Research-Solid Earth 125*, doi:
899 10.1029/2019jb018383.

900 Idrissi, H., Bollinger, C., Boioli, F., Schryvers, D., Cordier, P. (2016). Low-temperature
901 plasticity of olivine revisited with in situ TEM nanomechanical testing. *Science Advances*
902 *2,* 6, doi: 10.1126/sciadv.1501671.

903 Incel, S., Hilairet, N., Labrousse, L., John, T., Deldicque, D., Ferrand, T., Wang, Y.B., Renner,
904 J., Morales, L., Schubnel, A. (2017). Laboratory earthquakes triggered during
905 eclogitization of lawsonite-bearing blueschist. *Earth and Planetary Science Letters 459*,
906 320-331, doi: 10.1016/j.epsl.2016.11.047.

907 Isaak, D.G. (1992). High temperature elasticity of iron-bearing olivines. *Journal Of Geophysical*
908 *Research-Solid Earth 97*, 1871-1885, doi: 10.1029/91JB02675

909 Jessell, M.W., Bons, P.D., Griera, A., Evans, L. A., Wilson, C. J. L. (2009) A tale of two
910 viscosities, *Journal of Structural Geology 31*, 7, 719-736, doi: 10.1016/j.jsg.2009.04.010.

911 Jung, H., and Green H.W. (2004). Experimental faulting of serpentinite during dehydration:
912 Implications for earthquakes, seismic low-velocity zones, and anomalous hypocenter
913 distributions in subduction zones, *International Geology Review 46*(12), 1089-1102, doi:
914 10.2747/0020-6814.46.12.1089

915 Kaercher, P., Miyagi, L., Kanitpanyacharoen, W., Zepeda-Alarcon, E., Wang, Y., Parkinson, D.,
916 Lebensohn, R.A., De Carlo, F., Wenk, H.R. (2016). Two-phase deformation of lower
917 mantle mineral analogs. *Earth and Planetary Science Letters 456*, 134-145, doi:
918 10.1016/j.epsl.2016.09.030.

919 Karato, S.-i. (2008). *Deformation of Earth Materials: An Introduction to the Rheology of Solid*
920 *Earth.* Cambridge University Press, Cambridge.

921 Kranjc, K., Rouse, Z., Flores, K.M., Skemer, P. (2016). Low-temperature plastic rheology of
922 olivine determined by nanoindentation. *Geophysical Research Letters 43*, 176-184, doi:
923 10.1002/2015gl065837.

924 Kumamoto, K.M., Thom, C.A., Wallis, D., Hansen, L.N., Armstrong, D.E.J., Warren, J.M.,
925 Goldsby, D.L., Wilkinson, A.J. (2017). Size effects resolve discrepancies in 40 years of
926 work on low-temperature plasticity in olivine. *Science Advances 3*, doi:
927 10.1126/sciadv.1701338.

928 Li, L., Addad, A., Weidner, D., Long, H.B., Chen, J.H. (2007). High pressure deformation in
929 two-phase aggregates. *Tectonophysics 439*, 107-117, doi: 10.1016/j.tecto.2007.04.004.

930 Lin, F., Giannetta, M., Jugle, M., Couper, S., Dunleavy, B., Miyagi, L. (2019). Texture
931 Development and Stress-Strain Partitioning in Periclase plus Halite Aggregates. *Minerals*
932 *9*, doi: 10.3390/min9110679.

933 Long, H., Weidner, D.J., Li, L., Chen, J., Wang, L. (2011). Deformation of olivine at subduction
934 zone conditions determined from in situ measurements with synchrotron radiation.
935 *Physics of the Earth and Planetary Interiors 186*, 23-35, doi: 10.1016/j.pepi.2011.02.006.

936 Madi, K., Forest, S., Cordier, P., Boussuge, M. (2005). Numerical study of creep in two-phase
937 aggregates with a large rheology contrast: Implications for the lower mantle. *Earth and*
938 *Planetary Science Letters 237*, 223-238, doi: 10.1016/j.epsl.2005.06.027.

939 Mei, S., Suzuki, A.M., Kohlstedt, D.L., Dixon, N.A., Durham, W.B. (2010). Experimental
940 constraints on the strength of the lithospheric mantle. *Journal of Geophysiscal Research*
941 *115*, B08204, doi: 10.1029/2009jb006873.

942 Merkel, S., Hilairet, N. (2015). Multifit/Polydefix: a framework for the analysis of polycrystal
943 deformation using X-rays. *Journal of Applied Crystallography 48*, 1307-1313, doi:
944 10.1107/s1600576715010390.

945 Merkel, S., Tome, C., Wenk, H.R. (2009). Modeling analysis of the influence of plasticity on
946 high pressure deformation of hcp-Co. *Physical Review B 79*, 064110, doi:
947 10.1103/PhysRevB.79.064110.

948 Montési, L. G.J. (2013). Fabric development as the key for forming ductile shear zones and
949 enabling plate tectonics, *Journal of Structural Geology 50*, 254-266, doi:
950 10.1016/j.jsg.2012.12.011.

951 Montési, L. G. J., Hirth, G. (2003). Grain size evolution and the rheology of ductile shear zones:
952 from laboratory experiments to postseismic creep, *Earth and Planetary Science Letters*
953 *211* (1–2), 97-110, doi: 10.1016/S0012-821X(03)00196-1.

954 Morales, L.F.G., Mainprice, D., Kern, H. (2018). Olivine-antigorite orientation relationships:
955 Microstructures, phase boundary misorientations and the effect of cracks in the seismic
956 properties of serpentinites. *Tectonophysics 724*, 93-115, doi: 10.1016/j.tecto.2017.12.009.

957 Nishii, A., Wallis, S.R., Mizukami, T., Michibayashi, K. (2011). Subduction related antigorite
958 CPO patterns from forearc mantle in the Sanbagawa belt, southwest Japan. *Journal of*
959 *Structural Geology 33*, 1436-1445, doi: 10.1016/j.jsg.2011.08.006.

960 Padron-Navarta, J.A., Tommasi, A., Garrido, C.J., Sanchez-Vizcaino, V.L. (2012). Plastic
961 deformation and development of antigorite crystal preferred orientation in high-pressure
962 serpentinites. *Earth and Planetary Science Letters 349*, 75-86, doi:
963 10.1016/j.epsl.2012.06.049.

964 Passchier, C. W. and Trouw, R. A. J., Microtectonics, 2nd revised and enlarged edition, cop.
965 2005, Springer. ISBN 3-540-64003-7

966 Peters, J.F., Muthuswamy, M., Wibowo, J., Tordesillas, A. (2005) Characterization of force
967 chains in granular material, *Physical Review E 72*, (4), 041307, doi:
968 10.1103/PhysRevE.72.041307

969 Proctor, B., Hirth, G. (2016). "Ductile to brittle" transition in thermally stable antigorite gouge at
970 mantle pressures. *Journal of Geophysical Research-Solid Earth 121*, 1652-1663, doi:
971 10.1002/2015jb012710.

972 Proietti, A., Bystricky, M., Guignard, J., Béjina, F., Crichton, W. (2016). Effect of pressure on
973 the strength of olivine at room temperature. *Physics of the Earth and Planetary Interiors*
974 *259*, 34-44, doi: https://doi.org/10.1016/j.pepi.2016.08.004.

975 Raterron, P., Wu, Y., Weidner, D.J., Chen, J. (2004). Low-temperature olivine rheology at high
976 pressure. *Physics of The Earth and Planetary Interiors 145*, 149, doi:
977 10.1016/j.pepi.2004.03.007

978 Raterron, P., Merkel, S., Holyoke III, C.W., Axial temperature gradient and stress measurements
979 in the deformation-DIA cell using alumina pistons (2013) Review of Scientific
980 Instruments 84, 43906, doi: 10.1063/1.4801956

981 Regenauer-Lieb , K. and Yuen, D. A. (2008). Multiscale Brittle-Ductile Coupling and Genesis of
982 Slow Earthquakes, *Pure and applied geophysics 165,* 523–543, doi: 10.1007/s00024-008-
983 0326-8

984 Schmidt, M.W., Poli, S. (1998). Experimentally based water budgets for dehydrating slabs and
985 consequences for arc magma generation. *Earth and Planetary Science Letters 163*, 361-
986 379, doi: 10.1016/s0012-821x(98)00142-3.

987 Schwartz, S., Allemand, P., S. Guillot, S. (2001) Numerical model of the effect of serpentinites
988 on the exhumation of eclogitic rocks: insights from the Monviso ophiolitic massif

(Western Alps), *Tectonophysics 342,* 1–2, 193-206, doi: 10.1016/S0040-1951(01)00162-7.

Schwartz, S., Guillot, S., Reynard, B., Lafay, R., Debret, B., Nicollet, C., Lanari, P., Auzende, A.L. (2013). Pressure-temperature estimates of the lizardite/antigorite transition in high pressure serpentinites. *Lithos 178*, 197-210, doi: 10.1016/j.lithos.2012.11.023.

Shao, TB; Zhou, YS; Song, MS; Ma, X; Zhang, L; Yao, WM; Dang, JX; Li, JF. (2021). Deformation of Antigorite and Its Geological Implications, *Journal of Geophysical Research-Solid Earth 126*, e2021JB021650, doi: 10.1029/2021JB021650

Shimada, M., Cho, A., and Yukutake, H. (1983). Fracture strength of dry silicate rocks at high confining pressures and activity of acoustic emission. *Tectonophysics 96*, 159–172.

Singh, A.K., Balasingh, C., Mao, H.K., Hemley, R.J., Shu, J.F. (1998). Analysis of lattice strains measured under nonhydrostatic pressure. *Journal of Applied Physics 83*, 7567-7575, doi: 10.1063/1.367872

Takeda, Y.T. (1998). Flow in rocks modelled as multiphase continua: application to polymineralic rocks. *Journal of Structural Geology 20*, 1569-1578, doi: 10.1016/s0191-8141(98)00043-1.

Thielmann, M., Golabek, G. J., Marquardt, H. (2020). Ferropericlase control of lower mantle rheology: Impact of phase morphology. *Geochemistry, Geophysics, Geosystems 21*, e2019GC008688, doi: 10.1029/2019GC008688

Tokle, L., Hirth, G., Liang, Y., Raterron, P., & Dygert, N. (2021). The effect of pressure and Mg-content on ilmenite rheology: Implications for lunar cumulate mantle overturn. *Journal of Geophysical Research: Planets 126*, e2020JE006494, doi: 10.1029/2020JE006494

Uchida, T., Funamori, N., Yagi, T. (1996). Lattice strains in crystals under uniaxial stress field. *Journal of Applied Physics 80*, 739-746, doi: 10.1063/1.362920.

Wada, I., Wang, K., He, J., and Hyndman, R. D. (2008), Weakening of the subduction interface and its effects on surface heat flow, slab dehydration, and mantle wedge serpentinization, *Journal of Geophysical Research-Solid Earth*, *113*, B04402, doi:10.1029/2007JB005190.

Wallis, S.R., Kobayashi, H., Nishii, A., Mizukami, T., Seto, Y. (2011) Obliteration of olivine crystallographic preferred orientation patterns in subduction-related antigorite-bearing mantle peridotite: an example from the Higashi–Akaishi body, SW Japan, *in* Prior, D. J., Rutter, E. H. & Tatham, D. J. (eds) Deformation Mechanisms, Rheology and Tectonics: Microstructures, Mechanics and Anisotropy. Geological Society, London, Special Publications, 360, 113–127, DOI: 10.1144/SP360.7

Wang, Y., Hilairet, N., Nishiyama, N., Yahata, N., Tsuchiya, T., Morard, G., Fiquet, G. (2013). High-pressure, high-temperature deformation of CaGeO3 (perovskite)±MgO aggregates: Implications for multiphase rheology of the lower mantle. *Geochemistry, Geophysics, Geosystems*, doi: 10.1002/ggge.20200.

Wang, Y.B., Lesher, C., Fiquet, G., Rivers, M.L., Nishiyama, N., Siebert, J., Roberts, J., Morard, G., Gaudio, S., Clark, A., Watson, H., Menguy, N., Guyot, F. (2011). In situ high-pressure and high-temperature X-ray microtomographic imaging during large

deformation: A new technique for studying mechanical behavior of multiphase composites. *Geosphere 7*, 40-53, doi: 10.1130/ges00560.1.

Xia, G. (2013). *Experimental Studies on Dehydration Embrittlement of Serpentinized Peridotite and Effect of Pressure on Creep of Olivine* (doctoral dissertation). University of California, Riverside, USA.

Zha, C.S., Duffy, T.S., Downs, R.T., Mao, H.K., Hemley, R.J. (1996). Sound velocity and elasticity of single-crystal forsterite to 16 GPa. *Journal Of Geophysical Research-Solid Earth* 101, 17535-17545, doi: 10.1029/96JB01266

References From the Supporting Information

Druiventak, A., Trepmann, C.A., Renner, J., Hanke, K. (2011). Low-temperature plasticity of olivine during high stress deformation of peridotite at lithospheric conditions — An experimental study. Earth and Planetary Science Letters 311, 199-211, doi: https://doi.org/10.1016/j.epsl.2011.09.022.

Lloyd, G. E., Farmer, A. B., Mainprice, D. (1997) Misorientation analysis and the formation and orientation of subgrain and grain boundaries, Tectonophysics, 279, 1-4, 55-78, doi: 10.1016/S0040-1951(97)00115-7

Long, H., Weidner, D.J., Li, L., Chen, J., Wang, L. (2011). Deformation of olivine at subduction zone conditions determined from in situ measurements with synchrotron radiation. Physics of the Earth and Planetary Interiors 186, 23-35, doi: 10.1016/j.pepi.2011.02.006.

Lutterotti, L., Bortolotti, M., Ischia, G., Lonardelli, I., Wenk, H.-R. (2007). Rietveld

texture analysis from diffraction images. Z Kristallogr. Suppl. (Suppl 26), 125–

130, doi: 10.1524/zksu.2007.2007.suppl_26.125

Mei, S., Suzuki, A.M., Kohlstedt, D.L., Dixon, N.A., Durham, W.B. (2010). Experimental constraints on the strength of the lithospheric mantle. Journal of Geophysiscal Research 115, B08204, doi: 10.1029/2009jb006873.

Proctor, B., Hirth, G. (2016). "Ductile to brittle" transition in thermally stable antigorite gouge at mantle pressures. Journal of Geophysical Research-Solid Earth 121, 1652-1663, doi: 10.1002/2015jb012710.

Proietti, A., Bystricky, M., Guignard, J., Béjina, F., Crichton, W. (2016). Effect of pressure on the strength of olivine at room temperature. Physics of the Earth and Planetary Interiors 259, 34-44, doi: https://doi.org/10.1016/j.pepi.2016.08.004.

Raterron, P., Wu, Y., Weidner, D.J., Chen, J. (2004). Low-temperature olivine rheology at high pressure. Physics of The Earth and Planetary Interiors 145, 149, doi: 10.1016/j.pepi.2004.03.007